Recent Advances and Current Trends in Transmission Tomographic Diffraction Microscopy

Nicolas Verrier, Matthieu Debailleul, Olivier Haeberlé

MDPI

Review

Recent advances, and current trends in transmission tomographic diffraction microscopy

Nicolas Verrier *, Matthieu Debailleul and Olivier Haeberlé

Institut Recherche en Informatique, Mathématiques, Automatique et Signal (IRIMAS UR UHA 7499), Université de Haute-Alsace, IUT Mulhouse, 61 rue Albert Camus, 68093 Mulhouse Cedex, France
* Correspondence: nicolas.verrier@uha.fr Tel.: +33 (0)3 89 33 76 66

Abstract: Optical microscopy techniques are among the most used methods in biomedical sample characterization. In their more advanced realization, optical microscopes demonstrate resolution down to the nanometric scale. These methods rely on the use of fluorescent sample labeling in order to break the diffraction limit. However, fluorescent molecules phototoxicity or photobleaching is not always compatible with the investigated samples. To come over this limitation, quantitative phase imaging techniques have been proposed. Among these, holographic imaging has demonstrated its ability to image living microscopic samples without staining. However, for 3D assessment of samples, tomographic acquisitions are needed. Tomographic Diffraction Microscopy (TDM), combines holographic acquisitions with tomographic reconstructions. Relying on a 3D synthetic aperture process, TDM allows for 3D quantitative measurements of the complex refractive index of the investigated sample. Since its initial proposition by Emil Wolf in 1969, the concept of TDM has found a lot of applications, and has become one of the hot topics in biomedical imaging. This review focuses on recent achievements in TDM development. Current trends and perspectives of the technique are also discussed.

Keywords: Holographic Microscopy; Tomography; Data Reconstruction; polarimetric/vectorial imaging; multiple scattering; Holography; Diffraction; Fourier Optics

1. Introduction

Optical microscopy is an essential tool for biomedical sample characterization. Historically limited by light diffraction, optical microscopy was the room for huge research efforts leading to super-resolution techniques, allowing structural imaging with a resolution down to a few nanometers [1–4]. However, these super-resolved methods rely on the use of a fluorescent labeling of the investigated sample, which can induce photobleaching, phototoxicity or can even interfere with the measured information [5–7].

Quantitative Phase Imaging (QPI) can be envisaged to circumvent these issues [8]. Several techniques like Fourier ptychography [9], short coherence interferometry [10], or Digital Holographic Microscopy (DHM) [11] have already been demonstrated. In the remainder of this article, we will focus on the extraction of phase information considering DHM.

DHM is based on the holographic concept proposed by Gabor in 1948 [12]. Instead of recording the image of the investigated object, one records the interference between a reference field (part of the light, which does not encounter the object), and the object field (part of the light that is scattered by the object). Recording was initially performed using high-resolution photographic plates. With the development and the democratization of digital sensors, photographic plates were replaced by imaging sensors for most of the current applications [13]. In this case, the analogue reconstruction step, consisting in positioning the hologram back in the illumination beam, is replaced by digital methods [14–16]. It should however be noted that, in its original implementation, holography suffers

Citation: Verrier, N.; Debailleul, M.; Haeberlé, O. Recent advances, and current trends in transmission tomographic diffraction microscopy. *Sensors* **2023**, *1*, 0. https://doi.org/

Received:
Revised:
Accepted:
Published:

from the so-called "twin-image" noise, resulting in a superimposition of the reconstructed object with its out-of-focus image.

This issue was tackled when Leith and Upatnieks introduced off-axis implementation of holographic acquisitions [17]. Here, the hologram is spatially modulated due to the off-axis interference, leading to a direct separation of real and twin-image information in the Fourier space. Coupling off-axis acquisitions with Fourier space filtering, therefore makes it possible to obtain amplitude and phase of the object field from a single holographic acquisition [18]. Phase-shifting interferometry has also been demonstrated as a mean to extract amplitude and phase of the object field [19]. Instead of introducing a spatial modulation, the reference beam is phase shifted with a constant phase step. Combining several acquisitions allows for suppression of the unwanted terms in the hologram distribution, thus allowing for the complex object signal extraction. However, even if conventional reconstruction methods allow to obtain a 3D information about both amplitude and phase of the field, the axial resolution is lost. As a matter of fact, information is integrated over the depth of field of the microscope objective [20].

Axial resolution can be brought back by tomographic acquisitions, as theorized by Emil Wolf in 1969 [21]. The framework proposed by Wolf makes it possible, from the combination of 2D holographic acquisitions, to reconstruct the three-dimensional distribution of the complex refractive index of the investigated sample, while accounting for diffraction of light at microscopic scale. The technique however needs heavy computational means, that were not available at that time. First implementations of the technique was reported by the team of S. Kawata in Japan [22–24]. Nevertheless, data reconstruction needed state of the art supercomputer to give effective results, which limited larger adoption of TDM. Reinterpretation of Wolf's original article made it possible for V. Lauer to build a TDM experiment relying on the use of a personal computer for data acquisition and processing [25]. Starting from this point, various implementations were proposed [26–32]. Note that the technique has been presented under various names: interferometric synthetic aperture microscopy, index of refraction tomography, tomographic diffraction microscopy, tomographic phase microscopy, phase tomography, optical diffraction tomography, holographic tomography, holotomography... Lateral resolution better than 100 nm has been demonstrated [32], however axial resolution is still limited by the "missing-cone" problem, well known in full-field microscopy, and illumination scanning tomographic configurations [33]. It should be noted that similar issues can be pointed out in sample rotation tomographic configurations [34]. Combining both illumination scanning and sample rotation is one of the solution to this missing frequencies problem [35]. Relying on this principle, enhanced axial resolution TDM [36], and isotropic resolution TDM [37] have been demonstrated.

TDM is a mature technology, and still an active field of research. Commercial devices are nowadays available [38–40]. This review discusses TDM theory, and presents most recent results involving either improvement in implementation, modification in the reconstruction methods, or in the image formation models. We also discuss the future of the technique, and the answers that TDM shall be able to bring to the present hot-topics in optical characterization of biological samples.

2. Tomographic diffraction microscopy

This section will be devoted to TDM principles. As TDM combines QPI, and tomographic acquisitions, within a 3D synthetic aperture scheme, both aspects will be derived.

2.1. General principles: Helmholtz equation and first-order Born approximation

Let us consider an object with a refractive index distribution $n(\mathbf{r})$ immersed in a medium whose refractive index is n_{imm}. Let $k_v = 2\pi/\lambda_v$ be the norm of the wavevector in vacuum. Wavevector in the immersion medium is therefore written as:

$$k_{\text{imm}} = k_v n_{\text{imm}} = \frac{2\pi n_{\text{imm}}}{\lambda_v}, \tag{1}$$

and

$$k(\mathbf{r}) = k_v n(\mathbf{r}), \tag{2}$$

for propagation in the sample of refractive index $n(\mathbf{r})$. Using an imaging sensor makes it possible to detect part of the "total" field $u_t(\mathbf{r})$, containing information about, both the field scattered by the object $u_s(\mathbf{r})$, and the illumination field $u_i(\mathbf{r})$ so that we can write:

$$u_t(\mathbf{r}) = u_s(\mathbf{r}) + u_i(\mathbf{r}). \tag{3}$$

The illumination field $u_i(\mathbf{r})$ is solution of the homogeneous Helmholtz equation, derived from Maxwell equations, and given by:

$$\left(\nabla^2 + k_{\text{imm}}^2\right) u_i(\mathbf{r}) = 0. \tag{4}$$

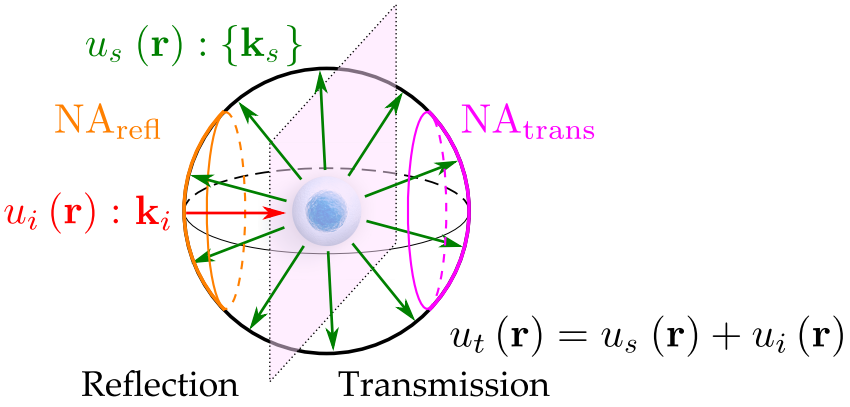

Figure 1. Geometrical interpretation of light diffraction within the first-Born approximation.

The total field $u_t(\mathbf{r})$, given Eq. (3), is also a solution of the homogeneous Helmholtz equation:

$$\left[\nabla^2 + k(\mathbf{r})^2\right] u_i(\mathbf{r}) = 0. \tag{5}$$

Combining Eqs. (4), and (5) using Eq. (3) leads to the expression of the total field as a function of the scattered field:

$$\left(\nabla^2 + k_{\mathrm{imm}}^2\right) u_s(\mathbf{r}) = -k_v^2 \left[n(\mathbf{r})^2 - n_{\mathrm{imm}}^2\right] u_t(\mathbf{r}). \tag{6}$$

Factorizing by n_{imm}^2 is the right hand side of Eq. (6), makes it possible to express the scattered field as a function of the object's scattering potential $\mathcal{V}(\mathbf{r})$:

$$\left(\nabla^2 + k_{\mathrm{imm}}^2\right) u_s(\mathbf{r}) = -k_{imm}^2 \left[\frac{n(\mathbf{r})^2}{n_{\mathrm{imm}}^2} - 1\right] u_t(\mathbf{r}) = -\mathcal{V}(\mathbf{r}) u_t(\mathbf{r}). \tag{7}$$

Solution of Eq. (7) is classically obtained by introducing the Green's function $\mathcal{G}(\mathbf{r})$ defined by:

$$\left(\nabla^2 + k_{\mathrm{imm}}^2\right) \mathcal{G}(\mathbf{r}) = \delta(\mathbf{r}), \tag{8}$$

$\delta(\mathbf{r})$ being the Dirac distribution. This methods allows expressing Eq. (7) as the following convolution product:

$$u_s(\mathbf{r}) = \int_V \mathcal{V}(\mathbf{r}') u_t(\mathbf{r}') \mathcal{G}(\mathbf{r} - \mathbf{r}') d\mathbf{r}', \tag{9}$$

where $\mathcal{G}(\mathbf{r} - \mathbf{r}')$ is the source of a spherical wave propagating in a medium of refractive index n_{imm}:

$$\mathcal{G}(\mathbf{r}) = \frac{1}{4\pi} \frac{e^{ik_{imm}|\mathbf{r}|}}{|\mathbf{r}|}. \tag{10}$$

However, determining $\mathcal{V}(\mathbf{r})$ from scattering field measurement is challenging as $u_s(\mathbf{r})$ is present in the two sides of Eq. (9). One possibility to circumvent this difficulty is to consider a weakly scattering object, thus simplifying Eq. (3):

$$u_t(\mathbf{r}) = u_s(\mathbf{r}) + u_i(\mathbf{r}) \approx u_i(\mathbf{r}). \tag{11}$$

This constitutes the so-called first-order Born approximation. Within this framework, Eq. (9) is written:

$$u_s(\mathbf{r}) = \int_V \mathcal{V}(\mathbf{r}') u_i(\mathbf{r}') \mathcal{G}(\mathbf{r} - \mathbf{r}') d\mathbf{r}', \tag{12}$$

This imaging method can therefore be seen as a 3D linear shift-invariant filtering operations, which not only provides a powerful analysis tool, but also permits to compare it with other linear systems [41,42]. As we shall see, its simple geometric interpretation also provides an elegant illustration of the TDM aperture synthesis process. A Fourier space interpretation of Eq. (12) is proposed Fig. 1. The incident wavefield, represented by vector $\mathbf{k}_i$ (in red), is scattered by the

object. The scattered field $u_s(\mathbf{r})$ is associated with the set of vectors $\{\mathbf{k}_d\}$ (in green). The Ewald sphere (black) represents the domain within which light is scattered. Its radius is given by:

$$R_{\text{Ewald}} = \frac{2\pi n_{\text{imm}}}{\lambda_v}. \tag{13}$$

To complete the geometrical interpretation, we get back to Eq. (12), decompose the illumination field on the Green functions basis and express the Fourier transform of $\mathcal{V}(\mathbf{r})$ as a function of the scattered field spectrum:

$$\tilde{\mathcal{V}}(k_{ox}, k_{oy}, k_{oz}) = \frac{ik_{sz}}{\pi} e^{-ik_{sz}z} \tilde{u}_d(k_{sx}, k_{sy}), \tag{14}$$

where $k_{sx,y,z}$ are the coordinates of the scattered wavevectors $\mathbf{k}_s$, and $k_{ox,y,z}$ the coordinates of the object wavevector $\mathbf{k}_o$. Considering the first Born approximation, both vector sets can be linked by:

$$\mathbf{k}_o = \mathbf{k}_s - \mathbf{k}_i \tag{15}$$

Eqs. (14) and (15) show that the 3D spectrum of the object can be obtained from 2D measurements of the diffracted field. The coordinates $k_{sx,y}$ correspond to the back focal plane of the collection objective (equivalent to the spectrum of the scattered field), while the illumination coordinates $k_{ix,y}$ correspond to the specular spot in the same plane. The axial coordinates of both vectors are finally obtained by projecting the respective coordinates on the Ewald sphere so that:

$$k_{i,s_z} = \sqrt{R_{\text{Ewald}}^2 - k_{i,s_x}^2 - k_{i,s_y}^2} \tag{16}$$

However, as it can be noticed from Fig. 1, it is not possible to acquire the full Ewald sphere with a unique acquisition. Wavefield detection can either be done in transmission or in reflection configuration. Moreover, microscope objectives have a limited numerical aperture (NA), limiting the norm of the wavevectors that can be acquired to k_{max}:

$$k_{\text{max}} = \frac{2\pi \text{NA}}{\lambda_v}. \tag{17}$$

Therefore, illumination and scattered wavevectors coordinates should fulfill:

$$k_{i,s_{x,y}} \leq k_{\text{max}}, \tag{18}$$

which forms the so-called McCutchen pupil [43], as illustrated by the orange (reflection), and purple caps of sphere on Fig. 1, respectively. It should be noted that, within Born approximation, the scattered field $u_s(\mathbf{r})$ scales as the cosine of the phase. Therefore, the obtained phase is determined in the $]-\pi; \pi[$ interval, which is not compatible with objects thicker than λ_v.

2.2. General principles: Helmholtz equation and Rytov approximation

Rytov formalism has been proposed to overcome limitations of the first-Born approximation in terms of sample thickness. Here, the total field $u_t(\mathbf{r})$ is expressed as a complex phase $\varphi_t(\mathbf{r})$ [44]:

$$u_t(\mathbf{r}) = e^{\varphi_t(\mathbf{r})} = u_s(\mathbf{r}) + u_i(\mathbf{r}), \tag{19}$$

where $u_i(\mathbf{r}) = e^{\varphi_i(\mathbf{r})}$. The total field is also a solution to the homogeneous Helmholtz equation.

Let $\varphi_{\text{R}}(\mathbf{r})$ be the complex phase associated to the Rytov, under the assumption that $\varphi_{\text{R}}(\mathbf{r}) \approx \varphi_s(\mathbf{r})$, the latter can be expressed as:

$$\varphi_{\text{R}}(\mathbf{r}) = \ln\left(\frac{u_t(\mathbf{r})}{u_i(\mathbf{r})}\right) = \ln\left(\frac{\alpha_t(\mathbf{r})}{\alpha_i(\mathbf{r})}\right) + i[\Phi_t(\mathbf{r}) - \Phi_i(\mathbf{r})], \tag{20}$$

where $\alpha_{t,i}$ are the amplitudes of the measured- and illumination fields, respectively, while $\Phi_{t,i}$ denote their respective phases. Reconstruction in the Rytov approximation therefore generally requires a phase unwrapping procedure. Both approaches are in fact linked. Indeed, it has been proved that [44]:

$$\varphi_{\text{R}}(\mathbf{r}) = \frac{u_s^{(B)}(\mathbf{r})}{u_i(\mathbf{r})}, \tag{21}$$

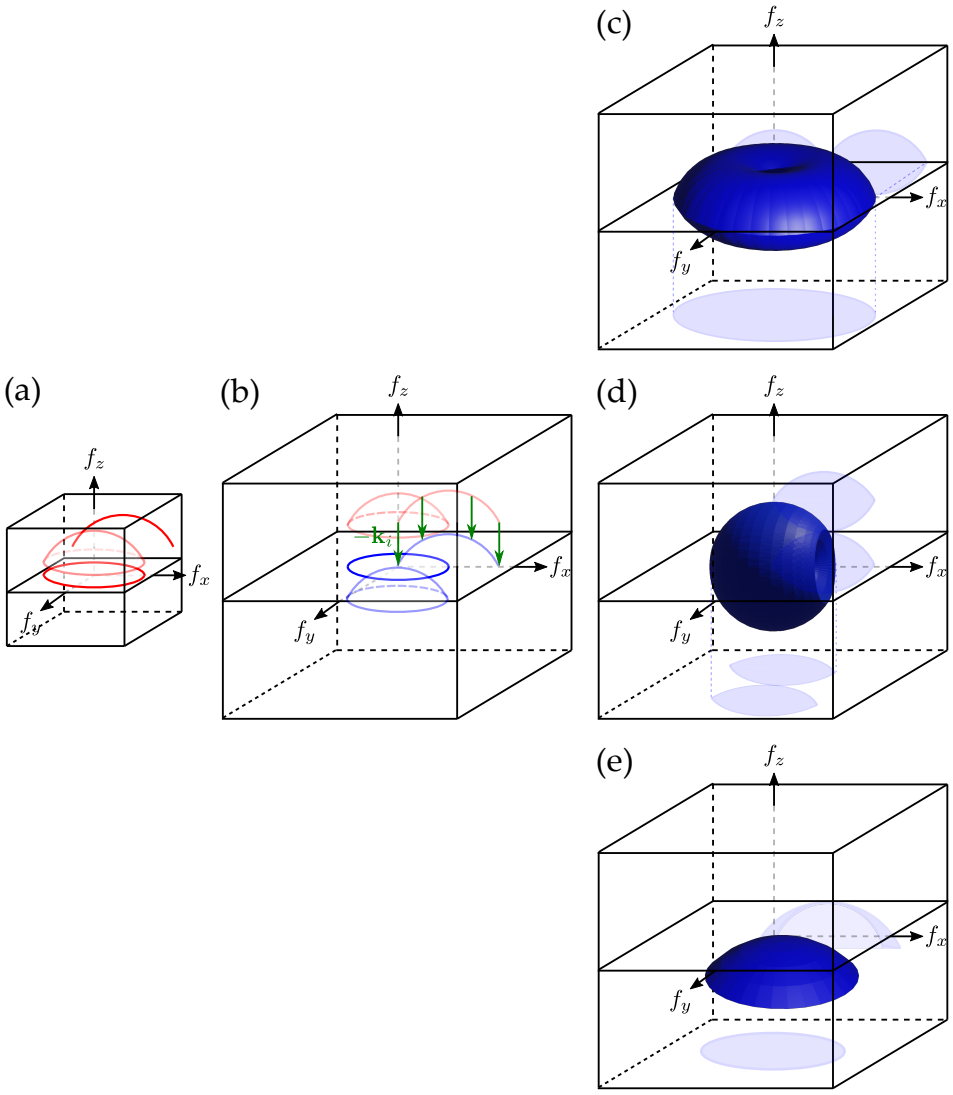

Figure 2. Illustration of the 3D synthetic aperture process. (a) Cap of the Ewald sphere collected. (b) Reallocation in a doubled in size Fourier space. Aperture synthesis with (c) illumination angle variation, (d) rotation of the object, (e) illumination wavelength variation.

with $u_s^{(B)}(\mathbf{r})$ the scattered field calculated under first-order Born approximation. Therefore, processing and reconstruction algorithms are common to both approaches. However, the range of validity is quite different: reconstructions under Rytov approximation are more robust with thick objects [45], and the general consensus is to use Rytov approximation in biological applications.

2.3. 3D aperture synthesis

As mentioned earlier, only a portion of the Ewald sphere is effectively collected. Enhancement of the spatial frequency content of the acquisition can be realized considering a 3D aperture synthesis scheme. It aims at combining, in Fourier space, acquisitions with variable object illumination conditions. Three common approaches can be envisaged for this task:

1. scanning the illumination over the object;
2. rotating the object within a fixed illumination;
3. varying the illumination wavelength.

These approaches are detailed Fig. 2. Note that here, we only focus on transmission TDM, the principles remaining the same for reflection TDM. The collected spectrum, (*i.e.* the set of acquired $\{\mathbf{k}_s\}$ wavevectors), is projected onto a cap of sphere using Eq. (16), as illustrated by Fig. 2(a). Then, according to Eqs. (14), and (15), the cap of sphere is reallocated in the Fourier space Fig. 2(b). The main difference between the three methods relies in the way the acquired content is reallocated. It should be noted that the same Optical Transfert Function (OTF) construction mechanisms can be applied to

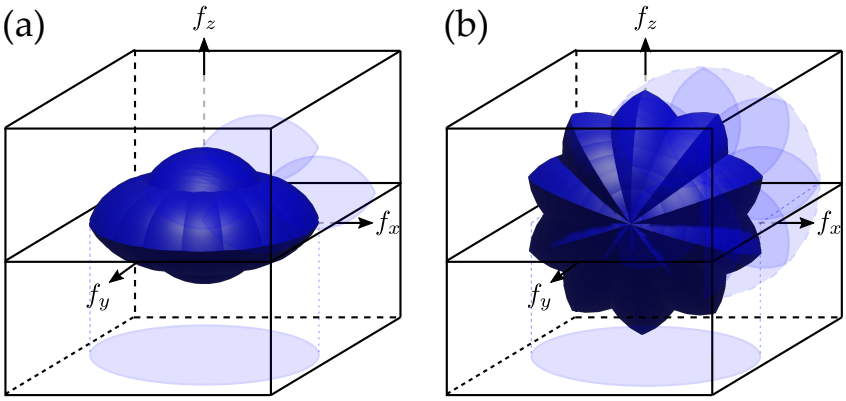

Figure 3. 3D synthetic aperture process with combined approaches. OTF obtained with (a) a full rotation of the sample combined with one illumination sweep, (b) an full illumination scan for a few object rotation angles.

reflection microscopy techniques, allowing to represent for instance image formation in interferometric microscopy, or Optical Coherence Tomography (OCT) [42,46].

2.3.1. 3D aperture synthesis with illumination sweep

In this configuration, the object is illuminated by a plane wave with a variable $\mathbf{k}_i$. As the sample remains fixed, this technique is particularly stable mechanically, resolving some of the problems encountered with sample rotation. Motorized mirrors, galvanometric scanners, or Digital Micromirror Devices (DMD), are routinely used for this task. The 3D spectrum is then built by subtracting the $\mathbf{k}_i$ contribution to the acquired spectrum (set of $\{\mathbf{k}_s\}$ vectors). The obtained Optical Transfer Function (OTF), as well as two orthogonal cuts in (x, y), and (x, z) planes, are depicted Fig. 2(c). One can notice that compared to holography Fig. 2(b), the frequency content is twice as large in the (x, y). Axial resolution is no longer limited to the thickness of the cap of sphere, but remains lower than the lateral one. Finally, one can notice a missing spatial frequency region. This is the so called “missing cone”, which is a phenomenon commonly occurring in full field transmission optical microscopy [47,48].

2.3.2. 3D aperture synthesis with sample rotation

Here, the illumination vector $\mathbf{k}_i$ is fixed, and the object is rotating. As a rotation of the object is equivalent to a rotation in the Fourier space, it is possible to reallocate the resulting spectra in the OTF proposed Fig. 2(d). Sample rotation can be performed by mechanical means [37,49,50], considering the sample self-motion in a confined environment [51,52], or considering optical trapping techniques [53]. Sample rotation gives an almost isotropic resolution, and with a maximal theoretical gain of $\sqrt{2}$ in terms of spatial frequency support [54–56], compared to holography. However, frequency support remains undefined along the axis of rotation of the sample, with the final spectrum exhibiting a so-called "missing apple core" around this axis [34]. In addition, this method requires a high number of angles, in order to properly sample the Fourier space, making registration between each hologram critical, possibly increasing sources of error at these scales.

2.3.3. 3D aperture synthesis with illumination wavelength variation

In this situation, both the object and the direction of the illumination wavevector $\mathbf{k}_i$ are fixed. As shown by Eqs. (13), and (17), for a given microscope objective, the Ewald sphere radius, and therefore the maximal accessible spatial frequencies are inversely proportional to the illumination wavelength in vacuum λ_0. Thus, taking several acquisitions at different wavelengths makes it possible to extend the frequency support [57–59]. One can in some configurations also use white-light illumination [60,61]. As illustrated Fig. 2(e), the frequency support is enhanced, but in this case the improvement is not as large as compared to the other synthesis methods.

2.3.4. 3D aperture synthesis with combined approaches

None of the presented approaches succeed in completely filling the OTF: illumination scanning results in a missing region along the light propagation axis, while missing frequencies can be noticed along the rotation axis when sample rotation is considered. However, what is interesting here is that these missing regions are not along the same axes. Therefore, combining both approaches should be beneficial. Theoretical demonstration of this concept has been presented by Vertu in 2011 [35], and recently, experimentally realized [36,37,62]. The OTF obtained with these approaches are

presented Fig. 3, with a full rotation of the sample combined with an illumination sweep Fig. 3(a) [35,36], and with a complete illumination sweep for a few sample rotation angles Fig. 3(b) [35,37,62].

2.3.5. Examples of achievement

In terms of experimental implementation of the technique, as well as achievements by various groups working in the field, the interested reader is referred to Refs. [8,63–69]. Figure 4 gives typical examples of realization with these various approaches. On the far left is an image of neural network obtained with 3D aperture synthesis with illumination sweep, adapted from Fig. 2 of Ref. [32]. In this paper, a 2D Sparrow resolution of about 75 nm was achieved, working at 405 nm illumination and using two N.A. = 1.4 numerical objectives as condenser and imaging objective. Sub-100 nm lateral resolution was obtained imaging a *Thalassiosira pseudonana* diatom frustule. These represent the highest obtained lateral resolution in TDM.

The second image, Figure 6 from Ref. [70], depicts the relative refractive index distribution in an HT-1080 cell, obtained with 3D aperture synthesis with sample rotation. In this experiment, cells are inserted inside a hollow fiber, where they grow in a similar way as in a Petri dish. The hollow fiber is rotated with a high-precision rotation stage, under the objective of a self-interference Digital Holographic Microscope (DHM), working at 532 nm, and using a 20×, N.A. = 0.4 long working distance (10 mm) objective. An isotropic subcellular resolution is demonstrated.

In order to obtain the highest-quality images, combined illumination sweeping and sample rotation can be used. This was achieved by [37] *et al.*, using a 1.4 NA illumination/detection system working at 633 nm, and attaching the observed specimens to an optical fiber, used as rotating sample holder. The image on the right shows Figure 4 from [37], which depicts a Betula pollen grain. This setup achieved an 3D isotropic resolution of about 180 nm. This image also illustrated the interest of imaging both refractive and absorptive components. Here, images (c)-(e) clearly show that absorption is mostly located on the inner wall of the pollen envelope.

Finally, far right image illustrates 3D aperture synthesis in so-called white-light tomography. Figure 4 of Ref. [59] is that of HT29 cells in false-colour rendering. A 350 nm lateral and a 900 nm axial resolutions have been obtained, lower than with the previous approaches, but still capable of revealing subcellular structures. The main advantage of this technique, is that the phase imaging module is an add-on, which can be attached to a regular optical transmission microscope, contrary to the previous techniques, requiring specific setups.

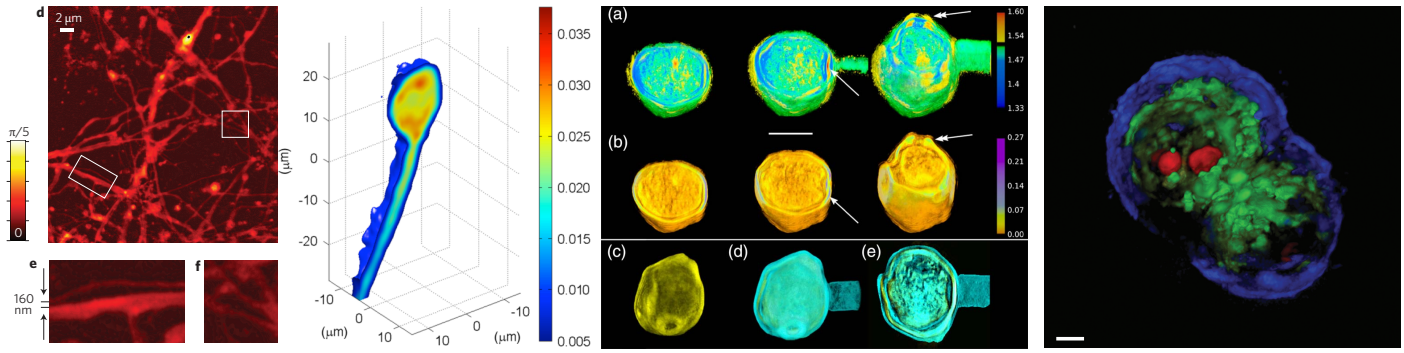

Figure 4. Examples of tomographic acquisitions with various systems. Far left: 3D aperture synthesis with illumination sweep, adapted from Fig. 2 of Ref. [32]. Super-resolved phase obtained by so-called 2π-DHM reveals the spatial order of a self-assembled neural network: full-field (d) and magnifications of regions outlined by white squares (e,f)). Left: 3D aperture synthesis with sample rotation. Figure 6 from Ref. [70] depicts the relative refractive index distribution in an HT-1080 cell with an extension, vertical cross sections through the cell. Refractive index peak to valley value $\Delta n = 0.032 \pm 0.004$. Right: 3D aperture synthesis with combined sample rotation and illumination sweep. Figure 4 from [37]. Betula pollen grain observed with TDM. Panels (a) and (b) show volumetric cuts (x–y views) through the 3D index of refraction image and absorption image, respectively. Note the higher index of refraction of the pollen walls, especially near the pores (double-headed arrow), and the double-layer outer wall (arrow). (c) Outer view of the pollen: image of the absorption component, displayed in yellow. (d) Outer view of the pollen: image of the complex index of refraction, with the refractive component displayed in cyan. (e) (x–y) cut through the pollen. Scale bar: 10 μm. Far right: 3D aperture synthesis in White-light tomography. Adapted from Fig. 4 of Ref. [59]. False-colour three-dimensional rendering of HT29 cells acquired in white-light tomography, z-stacks of 140 images. Scale bar 5 μm.

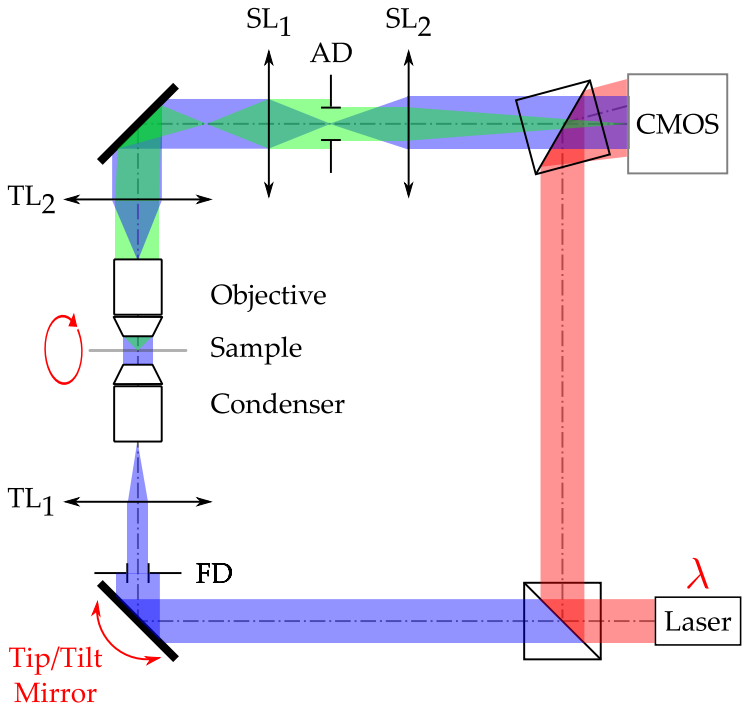

Figure 5. Sketch of a DHM configuration based on a Mach-Zehnder. FD: Field Diaphragm, AD: Aperture Diaphragm, TL: Tube Lens, SL: Sampling Lens. In red, part of the set-up that can be used to perform tomographic acquisitions.

2.4. Implementation

In order to perform refractive index resolved TDM measurements, having access to the phase of the light diffracted by the sample is mandatory. Phase can be obtained considering constrained reconstruction algorithms [71]. However, main TDM set-ups are based on DHM configurations, as illustrated Fig. 5. The illustrated DHM is based an a Mach-Zehnder interferometer. Light emitted by a laser is split into two distinct arms: the first one acts as a reference field (red on Fig. 5), while the second illuminates the investigated sample (blue) under a Köhler illumination. In other words, the optical system formed by TL_1, the condenser, the microscope objective, and TL_2 is an afocal device. With this configuration, the investigated sample is illuminated by a collimated wave, which allows the use of conventional reconstruction algorithms for further data processing [21]. Please note that in Fig. 5, the condenser is a microscope objective , as, for examples, in experiments described in [32,37,72,73]. Here, TL_1 grants light collimation on the investigated sample. The same can equally be done with a more conventional condenser, as long as the object remains illuminated by a plane wave. The light diffracted by the sample (green) is collected by an infinity-corrected microscope objective. Image of the investigated sample is formed by TL_2. For space/frequency space bandwidth product adjustment, one can consider the addition of an afocal device formed by lenses $SL_{1,2}$ between TL_2 image plane and the imaging sensor. Both illumination- and scattered fields are brought to interfere in the sensor plane. The sensor records the intensity of the diffracted field, given by :

$$\begin{aligned} I(x,y) &= |\mathcal{R}(x,y) + \mathcal{O}(x,y)|^2 \\ &= \underbrace{|\mathcal{R}(x,y)|^2 + |\mathcal{O}(x,y)|^2}_{\text{0 order}} + \underbrace{\mathcal{R}^*(x,y)\mathcal{O}(x,y)}_{\text{+1 order}} + \underbrace{\mathcal{R}(x,y)\mathcal{O}^*(x,y)}_{\text{-1 order}}, \end{aligned} \tag{22}$$

where $\mathcal{R}(x,y)$ is the reference field, and $\mathcal{O}(x,y)$ the field originating from the object arm. Extraction of both amplitude and phase of the object field is made possible by a modulation/demodulation process applied to the slowly varying envelope of the optical field. Modulation is either spatial or temporal. Spatial modulation has initially been proposed by Leith and Upatnieks [17]. Here, a spatial carrier frequency (cosine fringes) is "added" to the recorded interferogram's intensity, by making the three fields interfere with a slight angle, resulting in a separation of the three diffraction orders of Eq. (22) in Fourier space. Extraction/demodulation of the complex field $\mathcal{O}(x,y)$ is then performed by a pass-band filtering, associated with carrier compensation in the Fourier space [18]. Temporal modulation has also been proposed, and demonstrated by Yamagushi [19]. This method needs the acquisition of at least 3 holograms acquired with a properly phase-shifted reference wave. The phase shift is routinely introduced using frequency or phase modulation, for instance

brought by a mirror coupled with a piezoelectric transducer (PZT) [19], with an Electro Optic Modulator (EOM) [30], or an Acousto Optic modulator [74]. If one considers the acquisition of N holograms, a relative phase-shift of $2\pi/\mathrm{N}$ between each hologram has to be imposed. In this case, demodulation of the N hologram sequence can be performed by calculating:

$$I_{\mathrm{dem}}(x,y) = \frac{1}{\mathrm{N}} \sum_{k=0}^{\mathrm{N}-1} I_k(x,y) e^{-i\frac{2\pi k}{\mathrm{N}}}, \tag{23}$$

where I_{dem} is the demodulated field, and I_k is the k^{th} hologram of the sequence. It should be noticed that Eq. (23) is equivalent to a Fourier transform performed along the temporal axis (i. e. along the image sequence). For non-regular or random phase-shifts, one can apply a Principal Component Analysis (PCA) scheme on the acquired sequence [75,76].

Holographic microscopy can in fact be considered as a special case of simplification of tomography, with only one angle of illumination, the better-filled OTFs of tomographic systems being obtained by modifying the illumination conditions, then performing synthetic aperture. Nevertheless, it remains a method of choice for amplitude and phase extraction. From the experimental set-up presented Fig. 5, aperture synthesis can be performed by acting on the tip/tilt mirror (or other equivalent reflective beam scanning device), by rotating the sample within the illumination beam, or by modifying the illumination wavelength.

Angular scanning of the illumination beam is the most common implementation of the technique, even now commercially available [38,39]. To scan a focused beam in the back focal plane of the illumination optics, so as to deliver plane waves impinging onto the sample, stepper mirrors [25,30,31,77,78], fast tip-tilt membrane mirrors [37,72,79,80], galvanometric mirrors [27,81,82] or rotating prisms [23,32,83] have been used. Stepper mirrors allow for very large angular deflections, but are slow, and vibration sensitive. Membrane tip-tilt mirrors and galvanometric mirrors are much faster, galvanometric mirrors allowing for data acquisitions of several thousands of holograms per second, corresponding to acquiring about ten 3D images per second [84] (with an ultrafast camera and with post-reconstruction). In some cases, a rotating arm [85,86] has been used, performing azimuthal angular scanning ((with respect to the optical axis) with fixed polar angle (annular scanning [72]). The Nanolive tomographic microscope is based on this principle [38]. Conversely, scanning along the polar angle can also be used [87,88].

Spatial light modulators (SLMs) deflect a wave without mechanical motion, by directly acting on the wavefront phase of the illuminating beam, effectively allowing for beam angular scanning [89–93] or on the detected field [94]. Such systems are however slower than the fastest resonant galvanometric mirrors. Another technique for mechanical movement-free beam scanning uses matrix of micromirrors (Digital Micromirror Device or DMD). Micromirrors are binary components, which switch between 2 positions (deflecting or not deflecting the incident beam), so that a micromirror matrix effectively acts as a diffraction grating, which can be used to steer the illumination [95–98]. This however induces some constraints: it is mandatory to filter out unwanted diffraction orders to not perturb the illumination and the possible illumination directions are not continuous (as when using a galvanometric mirror or a tip-tilt mirror). The high-resolution tomographic microscopes developed by Tomocube, Inc. [39] take benefit of this approach. The concept of structured illumination has also been adapted to tomographic microscopy [90,99,100]. Note however that structured illumination diffraction tomography relies on a linear process with respect to field amplitude, while fluorescence structured illumination microscopy relies on a quadratic process with respect to field amplitude, so that the underlying image formation processes are fundamentally different [101]. Structured illumination in tomographic imaging in fact consists in multiplexing the illuminations, demultiplexing allowing for unmixing spatial frequencies, while in fluorescence imaging, it induces spacial frequencies spectrum extension, thanks to a multiplicative process in fluorescence-intensity image space, inducing convolution of spectra in Fourier space.

Alternately, one can also use a collection of light sources, corresponding to the desired illumination directions, and electronically controlled. The first implementation of this concept in tomographic imaging was made by Isikam *et al.* [102], but with a 1D scan only, and also using a lensless sensor. Extended to 2D angular scanning, this approach is very similar to optical ptychography in which phase and amplitude are not measured, but digitally reconstructed, as shown by Horstmeyer *et al.* [103].

Tomography by specimen rotation is less common, but presents some advantages, the most important one being that a standard holographic/phase microscope can be used, the price to be paid being the high-accuracy, compatible with interferometric measurements, sample rotations, which have to be performed (avoiding parasitic translations and conicity). Furthermore, in order to correctly fill the Fourier space, a large number of acquisitions is to be taken, each corresponding to an accurate rotation. In some cases, this approach is simplified when the sample itself can be directly rotated, without requiring specific preparation/manipulation. This is the case when observing optical- [37,104–106], or textile fibers [107,108]). For biological samples, they are usually encapsulated in a microcapillary [49,56,70], which serves

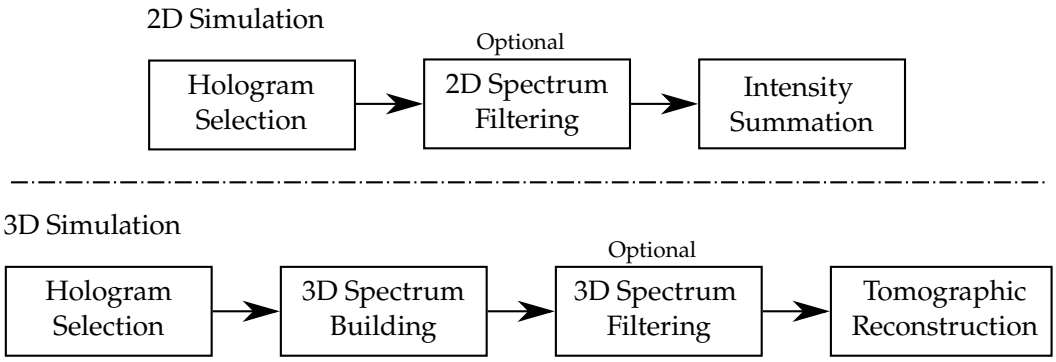

Figure 6. 2D and 3D simulation principles for multimodal reconstruction

to ensure sample rotation. While simplifying specimen rotation, note that the microcapillary may act as a cylindrical lens, distorting both illumination by the plane wave, as well as the detected image, which requires specific image reconstruction corrections [52]. Note that these drawbacks can be eliminated when the specimen is directly manipulated, with standard preparation between glass slide and cover glass, in a Petri dish, or when circulating through a microfluidic device [109]. This can be efficiently performed using optical tweezers [110], which have been adapted to perform microscopic tomography [53,111–113], the sole constraint being to perform an optically-induced rotation not around the optical axis z, but perpendicularly to this axis. Optical fibers can also be used to induce sample rotation [114,115]. Note that any phenomenon inducing a rotation of the sample can indeed be used to perform tomography with sample rotation. Dielectrophoresis (more precisely electrorotation) [116–118], when an external electric field induces sample rotation because it presents electrical potential variations, as well as acoustophoresis [119] (also known as sonophoresis or phonophoresis), acoustic manipulation of microscopic samples, have also been used in optical tomography [120].

Finally, as presented in Fig. 3, combining sample rotation with illumination rotation [35] permits to suppress the so-called "missing cone" characteristic of transmission microscope [47] as well as the residual "missing apple-core" of sample rotation tomography [34]. First attempt to conduct this proposal was performed imaging microfibers or attaching the sample to a micro tip used to rotate the specimen [37], but recently, optical tweezers have also been used, with configurations corresponding to Fig. 3(a) [35,36], or Fig. 3(b) [35,62].

One of the main flaw of TDM is its lack of selectivity in the reconstructed refractive index content. As a matter of fact, different class of structures can exhibits the same refractive information. This issue can be tackled by combining TDM with more conventional fluorescence labelled techniques [78]. Other imaging contrasts can also be investigated. Indeed, TDM allows for sequential acquisition of the optical field along various point of view of the sample, making it possible to mimic, by numerical means, conventional routine microscopes [121].

3. Data reconstruction and multimodal imaging

As TDM grants access to 3D information about the optical field scattered by the investigated sample, it can be used to mimic conventional microscope either in 2D, or in 3D [121–127]. Simulation schemes are depicted Fig. 6. Compared to conventional microscopy techniques, TDM performs sequential acquisitions of the optical field. Considering 2D microscopes, the general image formation model can be summarized as follow:

- Holograms that will be used for simulation are selected according to the illumination angle, which is equivalent to the illumination selection brought by the condenser in a conventional microscope ;
- Optional spectrum filtering can be envisaged. This is the numerical equivalent of the backfocal plane pupil filter that can be found in some specific microscope objectives. For instance, considering the case of Zernike phase-contrast microscopy [128] one can multiply the following pupil filter to the hologram Fourier transform:

$$\mathcal{P}\left(k_x,k_y\right) = \alpha\left(k_x,k_y\right)e^{i\Phi\left(k_x,k_y\right)}, \tag{24}$$

which allows both phase-shifting, and attenuation of the specular illumination contribution (part of the illumination beam that do not encounter the sample). In this situation, the attenuation can be defined as:

$$\alpha\left(k_x,k_y\right) = \begin{cases} \alpha & \text{if } \sqrt{\left(k_x-k_{i_x}\right)^2+\left(k_y-k_{i_y}\right)^2} \leq \rho_{\text{pc}} \\ 1 & \text{elsewhere} \end{cases}, \tag{25}$$

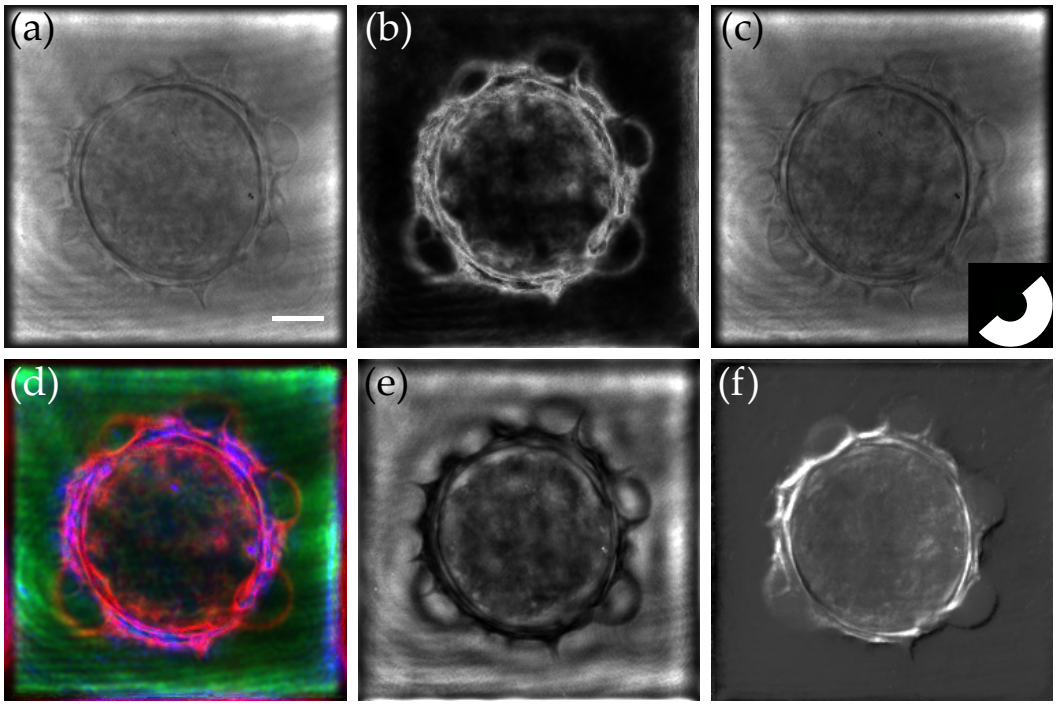

Figure 7. Simulated microscopy modalities. (a) Brightfield, (b) Darkfield, (c) Oblique illumination, (d) Rheinberg illumination, (e) Negative Phase-contrast, (f) DIC microscope. Scale bar is 10 μm. Adapted from Ref. [121]

with ρ_{pc} the radius of the pupil filter, and α the attenuation ratio. Here, the filter is centered on the specular illumination coordinate $\left(k_{i_x}, k_{i_y}\right)$. The same applies to the phase-shift Φ, which can be expressed:

$$\Phi\left(k_x, k_y\right) = \begin{cases} \Phi \text{ if } \sqrt{\left(k_x - k_{i_x}\right)^2 + \left(k_y - k_{i_y}\right)^2} \leq \rho_{\text{pc}} \\ 0 \text{ elsewhere} \end{cases} . \tag{26}$$

It should be noted that, in the case of Zernike phase-contrast, the condenser selects illumination angles along an annulus. Therefore, if we add all the processed holograms, the proposed filter will map an annulus in the Fourier space. This annulus is the perfect equivalent to the one existing in a phase-contrast microscope objective.

- Multiplexing of each processed hologram is finally performed by summing the calculated contrast intensity.

An example of multimodal reconstruction is showned Fig. 7 [121]. Here, using the scheme developed in Fig. 6, we were able to mimic the behavior of: (a) a brightfield, (b) a darkfield, (c) oblique illumination, (d) Rheinberg illumination, (e) negative phase-contrast, (f) Differential Interference Contrast (DIC) microscopes. More details about the simulation process can be found in Ref. [121]. Python version of our simulation and tomographic reconstruction codes can be found in Github [129].

It is also possible to extend the previous results to the third dimension. For this purpose, we built a specific scheme, presented Fig. 6, as an extension to the bidimensional case. Here, multiplexing is performed in the 3D Fourier space prior backfocal plane filtering. The final step is thus a conventional tomographic reconstruction. Obtained results, in both lateral, and axial cut are showned Fig. 8 for (a,f) darkfield, (b,g) phase-contrast, (c,h) DIC, (d,i) Rheinberg illumination microscopy. Cuts of the composite RGB Rheinberg spectrum are proposed for illustration purposes (e,j).

Note also that, at least for sample satisfying first Born approximation, real-time 3D acquisition/computation/display of high-resolution TDM images in augmented reality becomes a real possibility. Very fast cameras [84] and powerful GPU cards [130–135] are available, and have already been used for TDM. At present time, data transfer from the high-speed cameras to the GPU card may still constitute some bottleneck, but coupling with a holographic screen may in a near future open the path to live display of microscopic specimens in true 3D.

Finally, precise measurement of the electromagnetic field resulting from light-sample interaction not only allows for numerically recreate image formation in any type of optical microscope (using same illumination/detection numerical aperture), but also permits to numerically manipulate the optical properties of the sample itself. In this view, so-called

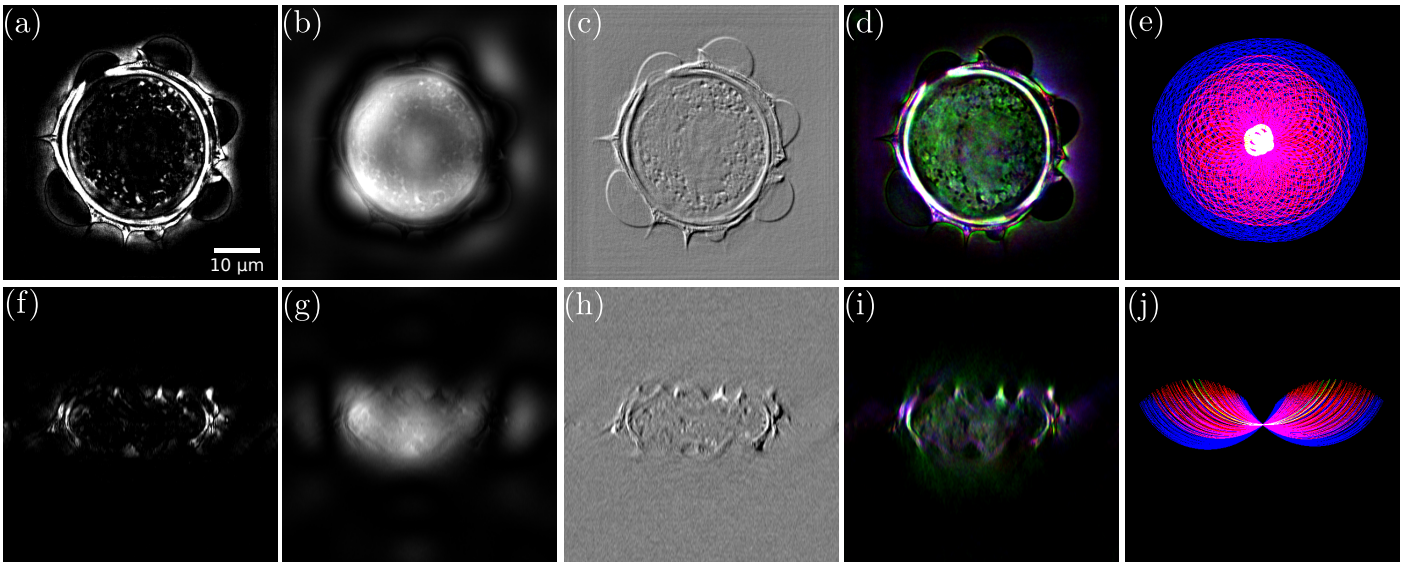

Figure 8. Simulated 3D microscopy modalities. (a-e) Lateral cuts, (f-j) axial cuts. (a,f) Darkfield, (b,g) Positive phase-contrast, (c,h) DIC microscope, (d,i) Rheinberg Illumination, (e,j) Rheinberg spectrum. Scale bar is 10 μm. Adapted from Ref. [121]

in silico clearing of the observed sample has been recently proposed to image highly scattering spheroids [136,137]. In this technique, layer-by-layer sample reconstruction allows for suppressing multiple scattering and sample-induced aberration from one layer in order to reconstruct the next layer, providing a numerical equivalent of chemical tissue clearing [138].

4. Advanced reconstruction methods

The description of the system obtained in "classical" TDM is based on the scalar Helmholtz equation (direct problem) and on the weak scattering hypothesis (inverse problem). Under these conditions, the field is linearly related to the refractive index via the Born or Rytov approximation. The system can be described by its Optical Transfer Function (OTF) in Fourier space, or, equivalently, by its Point Spread Function (PSF) in image space. As explained above, it provides a set of elegant and powerful tools: it gives a simple geometric description of the system, and allows performances to be compared with other devices thanks to the OTFs, such as reflection tomographic diffraction microscopy, interferometric microscopy, OCT ... [42,46].

However, these approximations can be challenged by thick samples or samples with a high refractive index contrast. Refraction modifies the illumination wave, and the plane wave hypothesis degrades with depth. Multiple scattering is ignored, which can lead to severe reconstruction problems.

Apart from the reconstruction artefacts (morphology, index or absorption values) induced by these effects, taking account of multiple scattering could in some cases even increase resolution beyond the classical limits. Although it remains an open debate, one explanation is that evanescent waves generated in an inhomogeneous medium are converted into propagating waves by multiple scattering. Since evanescent waves can contain subwavelength information, multiple scattering could encode super-resolution in far-field diffraction information [139,140]. It should be noted though, that in MTD, these improvements in resolution appear to be closely dependent on the experimental configuration [141].

4.1. Iterative reconstructions

Inversion methods based on non-linear models can include these effects to improve the reconstruction. To find the refractive index n at each pixel in a set Ω, the inversion scheme generally relies on a optimisation based method, where a cost function $\mathscr{C}(n)$ is minimized [142,143] :

$$\hat{n} = \underset{n\in\Omega}{\operatorname{argmin}}\{\mathscr{C}(n)\} = \underset{n\in\Omega}{\operatorname{argmin}}\{\mathscr{D}(n) + \tau\mathscr{R}(n)\} \tag{27}$$

$\mathscr{D}(n)$ measures the fidelity of the forward model to data, generally calculated over the P illumination angles with a l_2 norm:

$$\frac{1}{P}\sum_{p=1}^{P}\|\hat{m}^p - m^p\|_2^2 \tag{28}$$

The estimated scattered field $\hat{m}$ is calculated with the forward model, and compared to the measured scattered field m, to

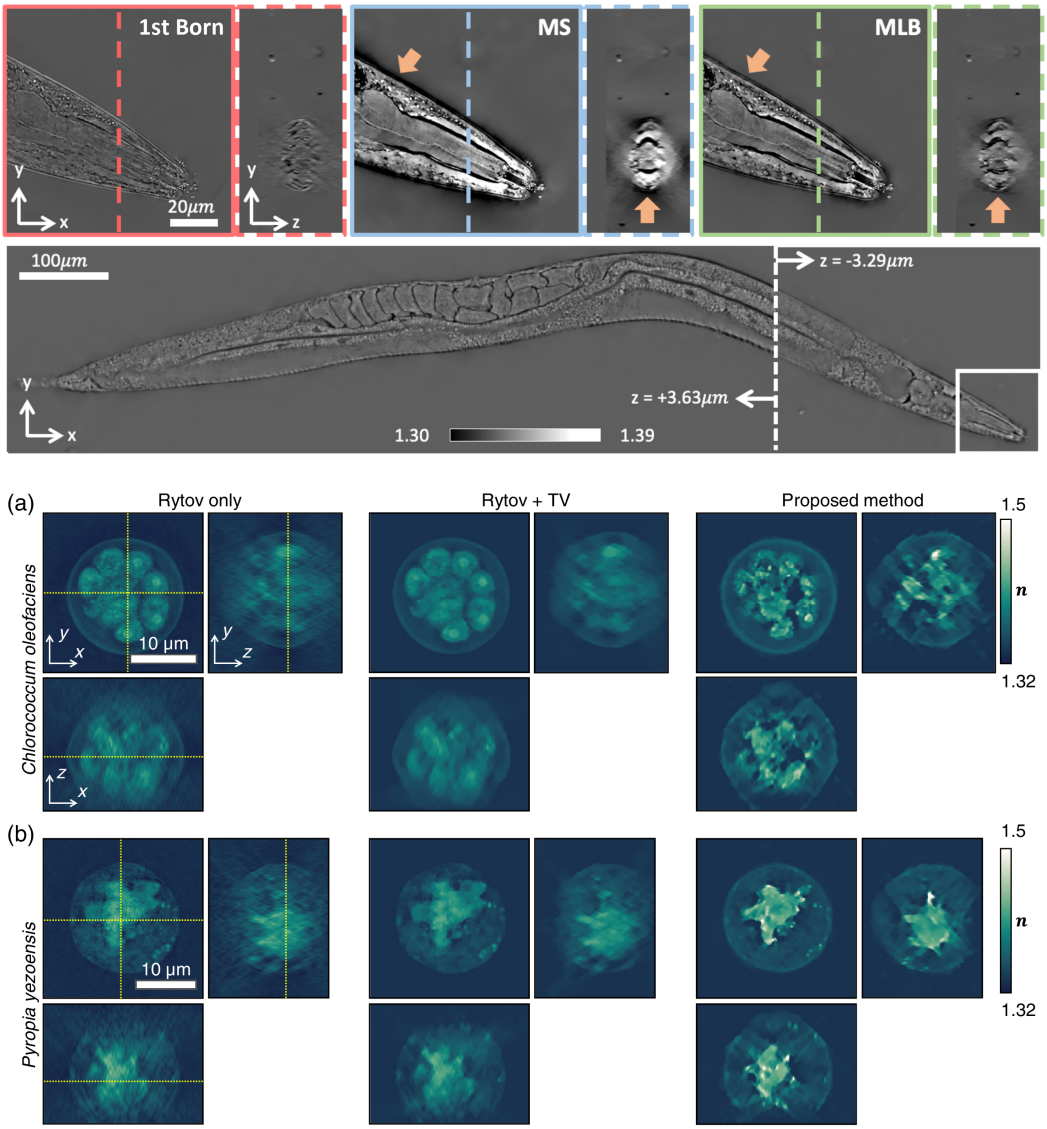

Figure 9. Top: Figure 6 from Ref. [144]: 3D refractive index reconstructions of an entire adult hermaphrodite C. elegans worm from the dataset of Ref. [145], using MLB model. The insets show zoomed-in comparison between orthonormal cross-sections using the first Born, multi-slice (MS), and MLB methods, for the white box region that includes the mouth and pharynx of the C. elegans. Bottom: Adapted from Figure 4 from Ref. [146]: reconstruction results of optically thick specimens: (a) *Chlorococcum oleofaciens*, and (b) *Pyropia yezoensis*. Each column represents cross-sectional images reconstructed by the Rytov approximation (first column), Rytov approximation with Total Variation regularization (second column), and the new method proposed in [146] (third column).

obtained the data fidelity term. The problem being generally ill-posed, a regularisation term $\mathscr{R}(n)$ is added to the data fidelity term [147] whose weight is adjusted by the parameter τ.

The direct model can be very general, avoiding the approximations of analytical approaches. It can also be formulated with intensity measurements, simplifying the experimental set-up [144,148,149]. Figure 9 top row (Figure 6 from Ref. [144]) illustrates the superior results obtained when reconstructing a rather large sample, an entire adult *C. elegans* worm when using a multi-layer Born multiple-scattering approach, compared to simple inversion based on first Born approximation, or multi-slice beam propagation method.

4.2. Forward models

The accuracy of the forward models is crucial, and mainly limited by computational power and memory limit. Rigorous solutions of the Maxwell equations can be calculated by FDTD or finite elements methods, providing a

ground truth for simulations and testing lighter algorithms [150,151], but their complexity is still prohibitive in iterative algorithms. In TDM, early works using advanced non-linear models (coupled dipole, contrast source inversion) were done in reflection TDM, with simple geometric object and limited field of view [152]. They showed the possibility to improve a lot the reconstructions, even beyond Abbe's limit [153].

The choice of a direct model is therefore often based on a compromise between accuracy and reconstruction speed.

4.2.1. Multi-layer models

An interesting approach is to divide the object into thin slices and apply an operator that calculates the effects of diffraction and refraction by the 2D refractive index map inside this slice. The total wave at the output of one layer becomes the illumination of the next one.

The calculation of the complex field at the next layer, $u(x, y, z + \Delta z)$, can be done using the beam propagation method (BPM) [154,155], in paraxial version [142,145,156], or improved versions [150,157]:

$$u(x, y; z + \Delta z) \propto F_{2D}^{-1}\left\{ F_{2D}\{u(x, y; z)\} \exp\left(-i\frac{k_x^2 + k_y^2}{k + k_z}\Delta z \right) \right\} \times \exp\left(i\frac{k_v \Delta n(x, y; z)\Delta z}{\cos\theta_i} \right) \tag{29}$$

where θ_i is the illumination angle, Δz the layer thickness, F the 2D Fourier transform, $\Delta n(x, y; z)$ the refractive index contrast.

Under a small thickness approximation, as can be seen in Eq. (29), this method separates the refraction and the diffraction operators, which are successively applied in the direct (refraction) and Fourier (diffraction) space. This algorithm is potentially very fast when using GPU, since the calculations are carried out in 2D and can use Fast Fourier Transform (FFT).

However, it ignores reflection, and does not take into account index inhomogeneity in the diffraction operator. This last problem can be addressed with wave propagation method (WPM) [158,159]: instead of propagating the field in the mean refractive index (first term in Eq. (29)), a multiplication by the 2D ($N \times N$) refractive map of the current layer is done. The price to be paid is an increased complexity ($\sim N^2$) compared to BPM ($\sim N \log N$)), since FFT cannot be used anymore. Hybrid methods using both BPM and WPM have also been proposed to alleviate the problem [160]. It should be noted that WPM also ignores reflection and evanescent waves, at least in its original form [161].

A similar multi-layer approach using the first Born approximation has been proposed to take into account both multi-scattering and backscattered waves [144]. The complex field is calculated by sequentially applying the first Born scattering to each layer of finite thickness. When this 3D model is applied to 2D thin slabs, it is worth noting that the Green's function must be modified by an obliquity factor [162,163]. In each slice, the algorithm consists of 2 steps:

- propagation of the incident field (total field from the previous layer) with the angular spectrum method [164],
- calculation of the scattered field under the 1st Born approximation, i.e. convolution between the modified Green function and the product of the incident field by the potential (eq. 12 on the slice thickness).

Like the BPM method, this method is also potentially fast, since these calculations are carried out with 2D FFTs.

4.2.2. Full 3D models

More advanced, and more complex, forward models are based directly on the solution of the scalar Helmholtz equation, obtained from the Green's function theorem (Eq. (9)), i.e. the Lippman-Schwinger equation for the total field. This equation can be solved with iterative schemes, and have been applied successfully to 2D problems [149,165]. The iterative forward scheme on 3D arrays computation make them more demanding, requiring more computing power and memory than multislice models. Some work has then focused on reducing this cost, in order to apply it to 3D/larger structures [166].

An alternative is to use the classical Born series, which arises naturally from the solution under the first Born approximation. In order to improve this approximation, the total field obtained under the first Born approximation can be used as the incident field in Eq. (9). A recurrence relation is then defined between the different orders of scattering [167]:

$$u^{n+1}(\mathbf{r}) = u_i(\mathbf{r}) + \int_V u^n(\mathbf{r}')f(\mathbf{r}')g(\mathbf{r} - \mathbf{r}')d^3\mathbf{r}' \tag{30}$$

However, its practical use is limited by the convergence criteria, restricted to the case of small objects, or low scattering potential [168]. Recently, a modified Born series has been proposed to achieve convergence, regardless of the size and the refractive index contrast [169] and has been used as a forward model in TDM on 3D objects [146].

The convergent Born series has been extended to solve the full wave equation (Maxwell's equations) [170], which opens the way for solving the most complex problems, including multi-scattering and vectorial aspects of light.

Figure 9 middle and bottom rows (adapted from Figure 4 from Ref. [146]) demonstrate the higher-quality results obtained by Lee *et al.*, with an inverse problem approach using modified Born series to image optically-thick samples, compared to Rytov approaximation and Rytov approximation with Total Variation regularization.

5. Accounting for the vectorial nature of light

In its simpler implementation, TDM relies on a scalar- and paraxial resolution of the Helmholtz equation [21]. This formalism does not make possible to account for light polarization. In 2002, Lauer proposed a vectorial extension of the Born formalism [25], but still limited by the paraxial propagation assumption, i.e. considering $\nabla\nabla\cdot\mathbf{E}=0$ in the propagation equation. Vectorial and non-paraxial resolution of the Helmholtz equation has been demonstrated, leading to a complete formalism especially useful in situation were light propagation is no longer linear (e.g. in the presence of Kerr effect) [171]. Approaches presented in the previous section, based on coupled dipole [141], propagating approaches [142], or Born series decomposition [169,170] can also be considered to perform reconstruction beyond the scalar approximation.

Qualitative use of polarization, as a novel imaging contrast in biological sample, has recently been proposed for characterization of zebrafish embryo [172,173]. Here, conventional TDM images are acquired under two different illumination polarization directions making it possible to fuse refractive index information (transparent part of the fish) with a pseudo-birefringence contrast (manly associated with fish bones).

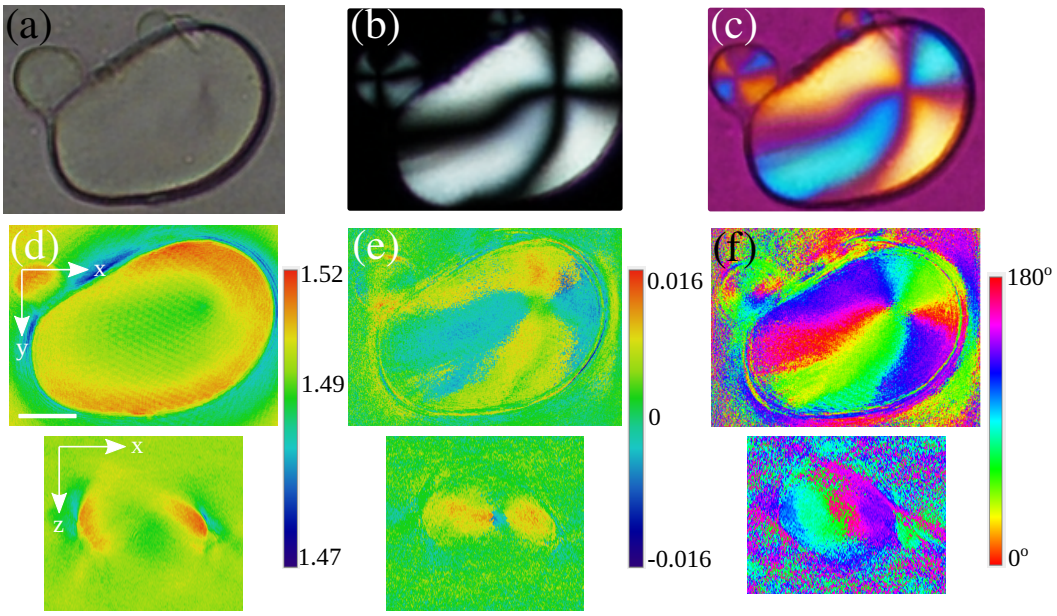

Figure 10. Polarization resolved acquisition of a potato starch. (a) Brightfield image. (b) Polarized Light Microscope (PLM) image. (c) PLM + phase plate image. (d) Refractive index map. (e) Birefringence map. (f) Polarization orientation map. Adapted from Ref. [73]

Quantitative extraction of polarization metrics has been recently demonstrated [73,150,174–176]. Here, considering a 2D approximated vectorial model (polarization of the sample is neglected along the light propagation axis) [73,150,175], or a full 3D-tensorial approach [176], the authors linked the reconstructed data to the Jones tensors of the sample. This is made possible at the cost of multiple tomographic acquisitions with varying illumination polarization scenarii. For instance, four TDM acquisition are needed if one consider linearly polarized illumination. These can be achieved using a single [150] or two [175] conventional cameras. Using a Polarization Array Sensor (PAS) as an image detector allows to divide the amount of acquisitions by a factor 2 [73]. Here, illumination and reference beams are circularly polarized. Polarization analysis is intrinsically performed by the PAS at the cost of data demosaicking and interpolation [177]. Example of quantitative polarization measurements, adapted from Ref. [73], are proposed Fig. 10. Here a potato starch is used as a birefringent sample. One can realize that polarization information is lost on both brightfield Fig. 10(a) and conventional TDM reconstruction Fig. 10(d). The well-known Maltese cross structure is made visible with a polarized light microscope (PLM) Fig. 10(b), and confirmed by the calculated birefringence map Fig. 10(e). A qualitative polarization orientation can be obtained by adding phase plate to the PLM Fig. 10(c), revealing a phase opposition

between two consecutive branches of the Maltese cross. This is confirmed by the quantitative polarization orientation measurement (f).

As mentioned earlier, method proposed in Ref. [73] implies an image demosaicking coupled with data interpolation. It should be noted that, due to the intrinsic structure of a PAS, coupled with the holographic nature of data acquisition, removing the interpolation for the data processing workflow is equivalent to perform 3D-DIC acquisitions [178]. This is a very interesting feature, indeed making PAS implementation of TDM a multimodal imaging technique.

6. Present and future trends

While the technique as been intensively investigated and improved, being now even commercially available, it still suffers from some limitations and/or complexity, which motivates new approaches in view of simplifying/ruggedizing its hardware implementation, accelerating the acquisitions, expending potential applications, or improving measurements reliability, which will necessitate implementing metrological approaches to index of refraction measurements.

6.1. Hardware simplification

For image reconstructions, TDM requires few tens to few hundreds acquisitions, depending on acquisition technique (illumination rotation, sample rotation, or both), reconstruction algorithms (simple direct inversion or more elaborate iterative methods), as well as targeted image quality and resolution. Sequential acquisition necessary to perform synthetic aperture by definition slows down image capture rate. This explains that for holographic acquisitions, off-axis setups [179] are preferred to phase-shifting approaches [19], which, while allowing for a larger field of view, require several intermediary acquisitions for each tomographic angle, even further slowing down the process. An optimal scanning pattern helps for minimizing the number of illumination angles to be used while keeping good image quality. Using 1-D line scanning allows for rapid acquisitions, but delivers non-isotropic resolution images, even in the x-y plane [87,180]. Star [30,77], circular [96,181], flower [31,37,78] or spiral [182] scanning patterns have been used. However, better filling of Fourier space is obtained with more elaborate scanning patterns [72,183–185] (note that the demonstration of the existence of an optimal scanning scheme, as well as its exact determination are still to be done). Preprocessing of the holograms [52,186], or implementation of adaptive illumination [91], for example to correct for residual aberrations, as well as data sorting to suppress bad quality data [187,188] also helps for keeping good image quality while trying to minimize the volume of acquisitions.

Data acquisitions however can be significantly accelerated by acquiring two multiplexed off-axis holograms [189], a technique which has been expanded to six-pack holography [190], and even so-called double six-pack holography, which allows for dynamic tomography by simultaneously acquiring 12 holograms arising from 12 angles of illumination [191]. In some cases, sample properties can be used to accelerate data acquisitions [192].

Snapshot tomography is another possible approach for multiplexing holograms, and accelerate acquisitions [193–196]. This method, compared to six-pack, or double six-pack holography, has the advantage of simplicity, by multiplexing the illumination using a microlens array, which translates onto the detection camera into many sub-apertures, each delivering an off-axis hologram corresponding to a different illumination angle. The price to be paid is however that each multiplexed hologram is captured with a much lower effective numerical aperture, while the six-pack approach makes optimal use of the objective numerical aperture.

Another approach to simplify hardware implementation of holographic tomography comes from that in its most common implementations, it require an interferometer to record holograms, which can be sensitive to vibrations or air flows, degrading the hologram quality. Common-path holography has been intensively developed to address these issues [197]. This approach has also been adapted to tomography. However, contrary to holography, the illumination direction changes, so that it requires a descanning galvanometer in order to compensate for the illumination beam direction and properly refocus it through a pinhole to regenerate a plane reference wave [198]. This added complexity has motivated other approaches, performing phase-shifting holography using a Spatial Light Modulator [181], or sharing interferometry via SLM [199], gratings [86,200] or polarizing elements [201]. These methods however require observing sparse samples, so as to use as reference beam a part of the illumination that has traversed an empty zone of the observed area. Alternately, one can use a wavefront sensor [202,203].

Another approach consists in recording intensity-only images, which are then numerically processed to reconstruct phase and amplitude images [71,204], to be properly recombined for tomography [205]. In such approaches, the hardware complexity of measuring both amplitude and phase of the diffracted field is transferred into software complexity of numerically reconstruction these quantities from intensity-only measurements. This explains that these approaches have long been hampered by the available computer power, but have experienced a growing interest in recent years [206–209], allowing for high-throughput imaging [210–212]. In recent years, approaches based on the transport of intensity equation

[213–217] or the Kramers-Kronig relations [121,218,219] have been developed, and multiple scattering [145,149,160,220] and polarisation sensitive [221] versions have also been implemented. Tomocube, Inc. [39] has now introduced a low-coherence light source tomographic system. For such approaches, deep-learning methods to recover the phase [222,223] appear particularly promising [224,225]. Note that as for holographic tomography, optimization of illumination in the case of partially-coherent [207,226,227] and incoherent intensity tomography [228–230]) is also of importance.

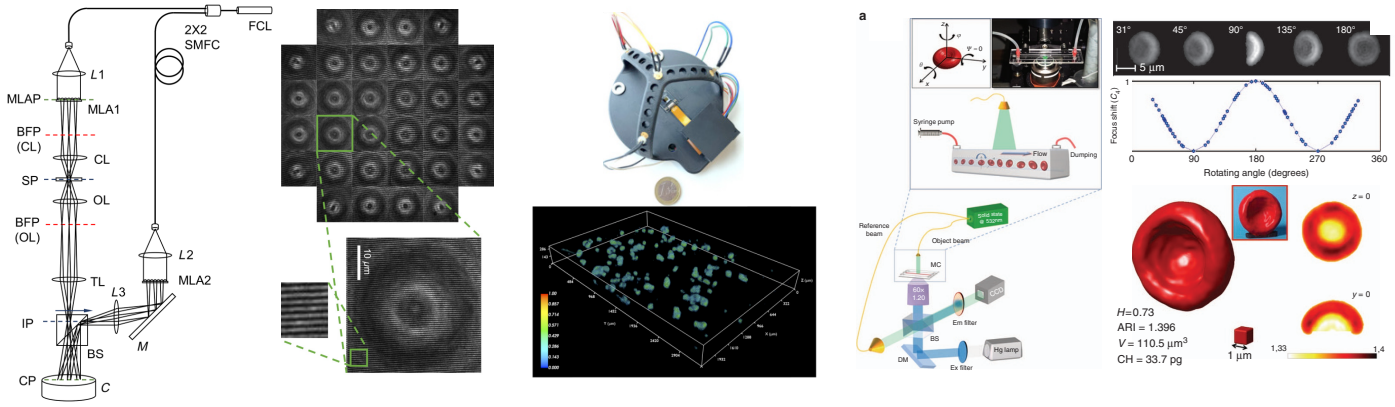

Figure 11. Examples of simplified tomographic setups. Left: snapshot tomography, adapted from Fig. 2 and Fig. 3 of Ref. [193]. Schematic diagram of the experimental setup: FCL, fiber- coupled laser; 2 × 2 SMFC, 2 × 2 single-mode fiber coupler; L1, L2, and L3, lenses; MLA1 and MLA2, microlens arrays; CL, condenser lens; OL, objective lens; TL, tube lens; BS, beam split- ter; M, mirror; C, camera; MLAP, MLA plane; BFP, back focal plane; SP, sample plane; IP, image plane; CP, camera plane. The raw interferogram image of Henrietta Lacks (HeLa) human-cervical-cancer cells consists of multiple projection images, one of which is enlarged on the right. Middle: lens-free tomographic microscope, adapted from Fig. 1 and Fig. 7 of Ref. [231]. Setup using only 4 illuminations and a CMOS image sensor and 3D reconstruction of intestinal organoids embedded in Matrigel over a volume of more than 3.4 mm × 2.3 mm × 0.3 mm. Color bar: normalized scattering potential. Right: tomographic flow microscopy, adapted from Fig. 1 and Fig. 2 of Ref. [232]. Sketch of the experimental R-TPM set-up. Cells are injected into a microfluidic channel and tumble while flowing along the y-axis. At the same time, a holographic image sequence is acquired. In the top-left corner of the inset, the reference system for cell tumbling is reported; in the top-right corner, a photo of the real set-up is shown. Rotation occurs around the x and z axes. BS, beam splitter; DM, dichroic mirror; MC, microchannel. Images of R-TPM, applied on RBCs presenting one-side concavity morphological anomalies (Ho0.9) with respect to the ideal healthy one. QPIs and mathematical dependence of the defocus coefficient from the rotation angle and the tomogram retrieved by the QPIs and the RI distributions at the z = 0 and y = 0 planes. ARI, V and CH are also reported together with the plastic 3D representations realized by a 3D printer.

Finally, lensless tomography [88,102,233] is another technique, which permits to avoid the use of an interferometer, by directly recording the interference fringes produced by the sample, deposited on, or very close to, the electronic sensor. Doing so leads to the simplest tomographic configurations, able to perform 3-D imaging of rather large samples (e.g. *C. elegans* nematode) using LEDs for illumination and without requiring focusing optics.

It is also interesting that in some cases, tomographic acquisitions can be performed without having to steer the illumination nor control sample rotation. This is the case for samples, which can freely rotate under peculiar conditions such as when flowing through microfluidic channels. This property of self-rotation has been cleverly used to image red blood cells and diatoms [232], human breast adenocarcinoma MCF-7 cells [234], identify cell nuclei [235], perform single cell lipidometry [236], or study yeasts [237]. Note that in fact, one can take benefit of any phenomenon inducing an uncontrolled rotation of the observed sample [238], if one is able to accurately recover the rotation angle, in order to properly reassign information for the reconstruction algorithm [239].

Figure 11 depicts three simplified tomographic systems, highlighting complementary approaches with specific advantages. Snapshot tomography [193,194,240] divides the objective numerical aperture using a microlens array to allow for simultaneously capture many views (Fig. 11, left). This approach is potentially the fastest for tomographic imaging, being only limited by the acquisition speed of the camera. Lens-free tomography (Fig. 11, center) simplifies the hardware by removing all the optical system for acquisition (microscope objective, interferometer), and using a limited number of LED illuminations. In [231], Luo *et al.* proposed a extreme simplification with only 4 illuminations and advanced reconstruction methods, allowing for imaging very large samples, with lateral dimensions in the millimeter range, and thickness of several hundreds of micrometers. Tomographic flow microscopy (Fig. 11, right) allows for using a simple holographic setup for data acquisition, the diversity of illumination being provided by natural sample rotation in

a microfluidic channel. The numerical difficulty for reconstruction is the correct estimation of the rotation angles, for which specific algorithms have been developed. They allow for efficient 3D image reconstruction, as illustrated by the image of a red blood cell exhibiting one-side concavity morphological anomaly.

6.2. Functionalization of tomography

Functionalization of TDM can be envisaged as the addition of new quantitative imaging contrast to the conventional refractive index modality. For this purpose, we already discussed, the "numerical functionalization" that can be brought by modifying data reconstruction as to mimic conventional microscope. This functionalization has also been proven to be possible by acting on the experimental set-up for accounting for sample polarizability.

While index of refraction measurements can be very precise and sensitive, and provides some chemical selectivity, they are however rather weakly discriminating, as different species/structures can exhibit same index of refraction when measured at single wavelength. But the optical index varies with wavelength, especially its absorption component. Up to now, absorption is simply neglected in commercial implementations of TDM, as well as in the vast majority of published research, which can be considered as surprising, but is linked to limited reconstruction models, or simplified acquisition systems. Hyperspectral systems have been developed to overcome this limitation [241,242]. In particular, Sung in [242] developed spectroscopic microtomography with a sensitivity high enough to distinguish, at the single cell level, oxygenated from deoxygenated red blood cells. Recently, hyperspectral tomography has been combined with SLM acquisitions [240,243].

Tomographic diffractive microscopy has been mostly developed in the visible range, but recently, a tomographic setup working in the near infrared has been developed by Ossowski, *et al.*, using as light source a tunable semiconductor laser, accordable from $\lambda = 800$ to 870 nm [244]. Note that such a short-coherence source necessitates the addition of an optical path difference adjustment module in the system. After proper calibration, this setup is able to identify specific structures related to colon cancer in unstained histologic sections, demonstrating the interest of working with near-infrared wavelength for tomographic approaches [244]. Using a similar approach, Juntunen *et al.* developed spectroscopic microtomography in the short-wave infrared, taking benefit from the much wider illumination spectrum provided by a supercontinuum laser, and from larger depth penetration possible in the SWIR range [245] to study large samples such as human hair and sea urchin embryos in various developmental stages.

Another promising approach to improve chemical sensitivity of holographic/tomographic imaging is based on recording phase/index changes induced by photothermal effects due to infrared absorption. It results a so-called bond-selective imaging, which has been successfully implemented in both interferometric- [246,247] and non-interferometric diffraction tomography [248,249], achieving sub-micrometer volumetric chemical imaging in individual cells, but also in model organisms such as *C. elegans* nematodes, but the technique has also been used for material studies [250].

Apart from chemical selectivity, one can also add structural selectivity by taking benefit of harmonic generation, characteristic of the structural architecture of the sample. Harmonic holography has been proposed about 15 years ago [251–258]. Tomographic extensions have also recently been studied [259–261], benefiting from the selectivity of second harmonic generation (SHG) to specifically identify non-centrosymmetric structures within the observed sample, and from the better resolution provided by synthetic aperture imaging. Its extension towards third harmonic generation (THG) could for example allow for identification of sub-micrometer specific structures (lipidic droplets for example [262]). Polarized SHG/THG is also sensitive to optical anisotropy, furthermore, SHG and THG often deliver complementary information about the sample [263].

In most TDM experiments, static or slowly moving objects are studied. Hugonnet *et al.* proposed an original approach for visualization of 3D refractive index dynamics. By appropriate spatial filtering of tomographic data, they are able to study slow and fast movements of subcellular organelles and biological molecules within living cells, which should help expanding the applications of index of refraction imaging [264].

Other dynamic information can be exploited. As a matter of fact, use of Doppler light broadening as already been demonstrated in the framework of digital holographic imaging for non-destructive testings [265,266], zebrafish blood flow assessment [267], or full retina quantitative blood flow imaging [268,269]. Extension to the third dimension have been demonstrated with a small number of illumination angle considering reconstruction of the blood flow under sparsity constrains [270,271]

Finally, use of phase contrast agents could allow for improving specificity, but obviously at the price of having to abandon working with unlabelled samples, which is the main advantage of the technique. As for fluorescence imaging, a genetically encodable phase contrast agent as been recently proposed [272], based on gas vesicles, used as biomolecular contrast agent easily identifiable using digital holographic microscopy.

6.3. Metrological approaches

An important point in view of a wider adoption of the technique will be the development of metrological approaches [273,274], so as to guarantee the validity and domain of confidence of measurements, which is especially important for material science and industrial applications. For biological investigations, the large natural variations between samples often lead to the need of averaging measurements, or only studying temporal variations within a same sample, and often relative measurements may suffice to distinguish sub-cellular compartments, for example lipids droplets having a higher index of refraction [236,275] than their surrounding cellular medium. The situation is often different when studying manufactured samples, such as optical fibres [37,104,276–278], photopolymerized structures [199,279] or plastic lenses [280], for which absolute measurements are often required to precisely characterize the sample properties both in terms of dimensions and optical index of refraction, for example to optimize a fabrication process. To do so, one often works using rather simple test samples such as calibrated beads, USAF [281] or Siemens [273] test patterns , but recently, more complex, true 3-D structures have been developed [282,283], in order to precisely characterize instrumentation performances [284]. Figure 12 (Figure 8 from Ref. [284]) illustrates the differences in shapes and optical refraction index measurements about the same sample when imaged with three different tomographic systems, highlighting the importance of developing standards in the domain.

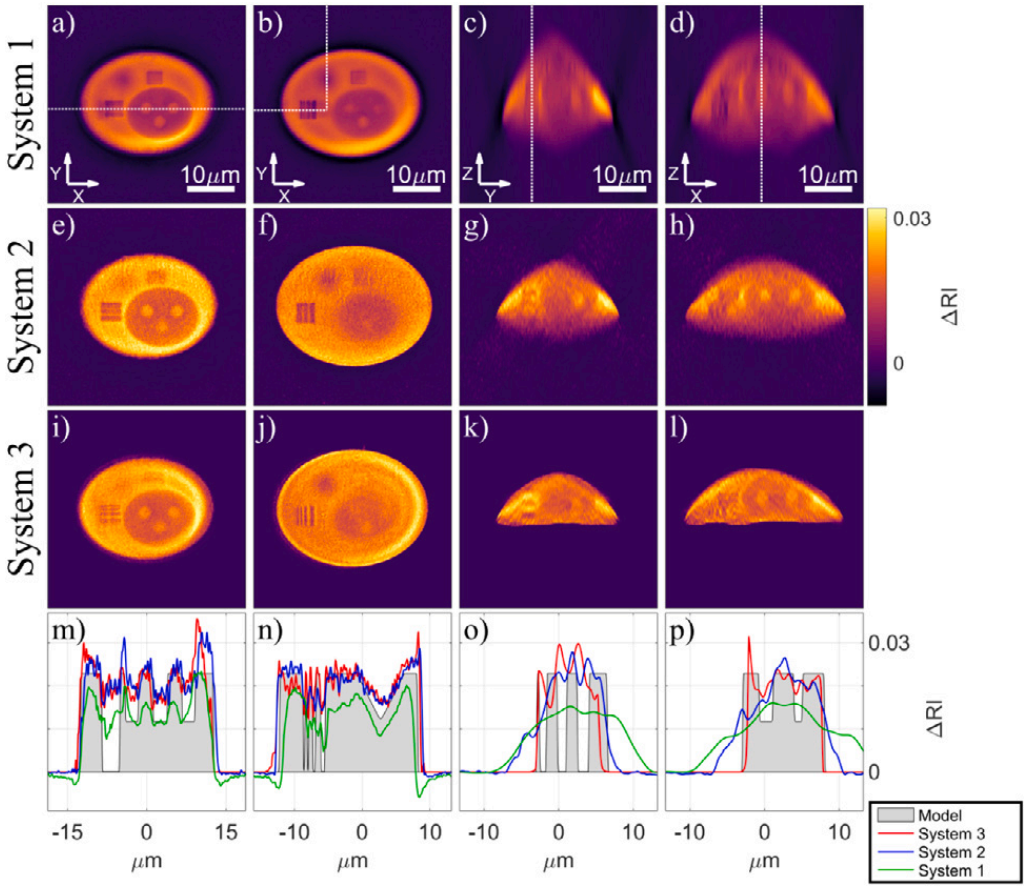

Figure 12. Use of an artificial cell for reconstruction accuracy assessment. Figure 8 From Ref. [284]: Cross-sections of the 3D RI distribution of the cell phantom measured experimentally in 3 LA ODT systems: (a–d) System 1, (e–h) System 2, (i–l) System 3. (m–p) RI profiles along the white dotted lines indicated on the corresponding panels (a–d).

Discrepancies in shape and/or measured index arise from restrictions in data acquisition (missing-cone problem, anisotropic resolution, and/or sub-optimal scanning schemes), limited accuracy (e.g. when large index of refraction differences are present within the samples, or between the sample and its immersion medium) or underlying simplifications (e.g. neglecting absorption) of reconstruction algorithms. A simple technique to avoid a too large index mismatch is to choose an immersion medium with index of refraction close to that of the observed sample, which is rather easy for artificial samples, but can even be performed in some cases for biological living specimens [285].

Note however that for the smallest structures, close to the limits of the instrument, the strong anisotropic resolution, characteristic of all transmission microscopes, will always constitute a problem: such minute structures are indeed then observed as elongated along the optical axis, which renders any volumetric measurements problematic (if one does not make supplementary assumptions such as that these structures are spherical for example). The importance of working with isotropic-resolution images is often overlooked: as even simple quantities such as volumes cannot be accurately measured at submicrometric scale in transmission microscopy, index of refraction, or species concentrations are even more difficult to estimate with precision, which motivates new developments to improve resolution.

6.4. Promising applications

As mentioned throughout this review, TDM has already found a lot of applications in various fields such as biomedical imaging, material science, surface characterization ...

In particular, the technique has been successfully used to study a large variety of samples in view of biological applications: red or white blood cells, hepatocyte cells, cancerous cells, neuronal cells, chromosomes, mechanisms of cell–cell or cell-to-surface adhesion, human hairs, but also to study bacteria, pollens, microalgae...See articles [8,64–68,286,287] and references therein. In fact, all applications for which phase imaging microscopy is successful [288,289] would benefit from the superior imaging capabilities of TDM, except (at least up to now) those requiring ultrafast imaging, such as high resolution imaging of erythrocytes vibrational modes [290], for which sequential acquisitions of data remain a big hurdle.

Note that applications have been greatly boosted by the availability of commercial implementations of the technique of TDM with illumination rotation or in white-light illumination. The interested reader will find numerous examples of applications on biological samples on the Nanolive [38], Tomocube [39] and PhiOptics [40] websites. The Nanolive system has the advantage to offer a large accessible space over the sample, while the Tomocube system allows for faster acquisitions at slightly higher resolutions. Both systems can also be upgraded with fluorescence imaging as an option. The white-light TDM of PhiOptics has been developed as a dedicated add-on module, with the advantage that this module can be fitted to a standard microscope body, allowing for a new imaging modality on an existing instrument.

These instruments also allow for high-throughput screening investigations, using 96-well plates, either directly added to the system (Nanolive, PhiOptics), or via a dedicated variant of the apparatus (TomoCube). Another promising approach for high-throughput screening is the so-called tomographic imaging flow cytometry [291], also developed in holographic version [232]. While limited to free-standing samples capable of spontaneously rolling through microfluidic channels, it offers a simple approach to study large number of individual cells, e.g. for lipidometric investigations [236], or to study nanoparticle internalization by cells [292]. TDM with sample rotation is another possible approach for high-throughput screenings of cells, when using a microcapillary to control cell flow and sample rotation under the objective [70]. Microfluidic channels can also be used [293,294]. But at present time, no from-the-shelf such system is yet available, limiting similar investigations to instrumentation development teams, while several companies offer holographic amicroscopes [295–298] or phase cameras [299], which could be used for such research.

Organoids or spheroids [300] are a hot topic in the community of optical imaging [301–303]. They however present specific difficulties, in terms of size, multiple diffraction and/or absorption, which challenges capabilities of current tomographic imaging systems, which have mostly been developed to work at the cellular level, and not at the tissue level. 3-D cell cultures [88,231] present similar challenges, so do animal models such as *C. elegans*. worm, Zebrafish or Xenopus frogs. Promising results on samples as large as Zebrafish embryos have indeed already been obtained [102,172,233,270,271,304]. Figure 13 (Adapted from Figure4(d) from Ref. [137] and Figure 5 From Ref. [172]) illustrates these large samples imaging capabilities. However, corresponding instruments are not yet deployed outside instrumentation laboratories, limiting their application, but the availability of tomographic microscopy techniques adapted to such biological system would certainly trigger a blooming of applications.

While most of TDM applications have been up to now in biological research, note that a growing interest appears in material sciences and micro-nanofabrication [37,104,199,276–280]. As mentioned in the *Metrological approaches* subsection, researches in these domains are often more demanding in terms of index of refraction calibration and absolute precision, which may explain that the technique is not as widely used as in biologigy, so that applications are less common. Situation is similar for holographic microscopy and tomographic microscopy in reflection mode, which have been less developed, and are not yet commercially available (with the noticeable exception of the Reflection DHM of LynceeTec [295]).

We however believe that forthcoming improvement of the technique will motivate dissemination of optical tomographic microscopy in these fields too, providing that some specific challenges, exposed in the next section, can be addressed.

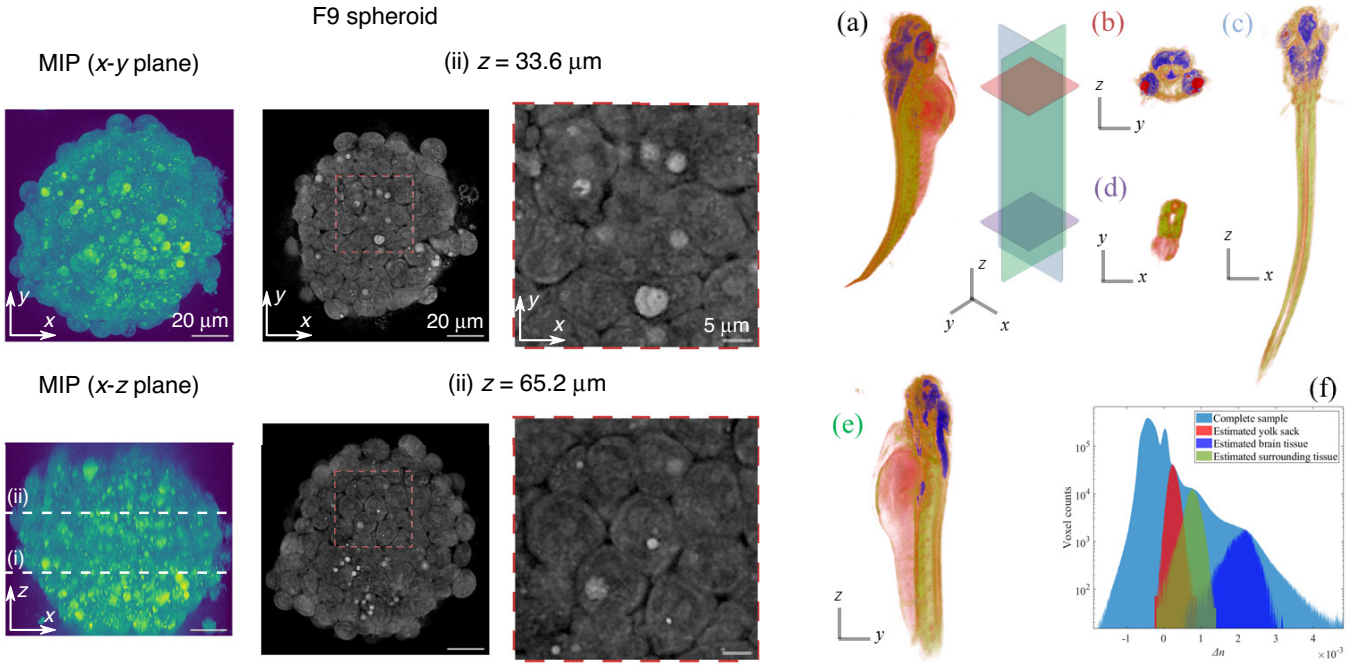

Figure 13. Examples of large sample tomographic imaging. Left: Adapted from Figure4(d) of Ref. [137]: RI tomography of F9 cell-type spheroids by in-silico clearing RI tomography. Maximum intensity projection (MIP) and cross- sections of RI maps. The depth of the cross-sections is denoted by white dashed lines in the MIP images. Right: Figure 5 From Ref. [172]: A 3D visualization of a complete zebrafish larva (3 days old) based on RI differences is shown in (a) and for different cross-sections in (b-e). In (f), a logarithmic plot is shown of the RI distribution of the complete sample (zebrafish larva and agarose). Indicated are the estimated Δn distributions of different types of tissue in the zebrafish larvae. The first two peaks in blue from the left are from the agarose and index matching liquid (BABB) contributions respectively.

6.5. Current Trends and Challenges

Optical microtomography has experienced tremendous development in the recent years. Many variants have been developed and tested, some having been commercially implemented. Nevertheless, several hurdles still exist, which motivates many groups to try pushing the performances of tomographic approaches even further.

As previously mentioned in the metrological approaches section, a strong limitation, when trying to quantify the volume and/or the index of refraction of the smallest sample details, comes from the anisotropic resolution of transmission optical microscopes. Combining illumination rotation and sample rotation delivers isotropic-resolution images [35,37,62], but this approach is limited to free-standing samples one can manipulate, and not, for example, for cells cultivated on a slide. Lauer [25] proposed adapting the so-called 4Pi configuration to tomographic approaches, performing both transmission and reflection acquisitions. Preliminary experiments have validated the concept of dual transmission and reflection acquisitions on semitransparent samples [281], but in this experiment, independent transmission and reflection reconstructions were performed, because no common data between transmission and reflection OTF could be acquired to perform synthetic aperture. Mudry *et al.* [305] proposed an elegant solution to this problem, with so-called mirror-assisted tomography, which in fact amounts to folding the 4Pi setup onto itself, thanks to the mirroring effect. Using the mirror effect allows for acquiring two transmission and two refection data set using only one objective and one camera. A simplified version has already been built [80] demonstrating that a reflection microscope can be used as a transmission microscope, but a full 4Pi configuration remains to be built. Zhou *et al.* proposed a similar concept in Ptychographic Diffraction Tomography, called opposite illumination [306], in which a transmission OTF (Fig. 2(c)), is combined with a reflection OTF with wavelength variation ([63], Fig. 10(c)), achieving quasi-isotropic resolution.

Another domain of possible progress remains the limited resolution. While fluorescence nanoscopy is now a reality, even commercially available, with routine resolution in the 50-100 nm range for biological applications, going down to a few nanometers in some cases, if one does not want or cannot use fluorescence labelling, performances and versatility are way lower. Resolution in far-field microscopy being limited by wave propagation, detection of evanescent waves by scanning near-field optical microscopy (SNOM) has been proposed [307], as well as so-called superlenses [308] or simply microspheres [309]. But all these approaches are based on near-field conversion/manipulation. Consequently, they are,

by definition, limited to surface imaging, and cannot deliver 3-D images of interior of transparent samples. Development of far-field optical microscopy with superresolved images is now a very active field (see for example [310–312] and references therein). In tomographic microscopy, most promising results have been obtained, up to now, in reflection configuration. Combining angular scanning and polarization [313] with advanced reconstruction algorithms taking into account multiscattering, has permitted to achieve a resolution of $\lambda/10$ in the far field [314]. Angular scanning and multispectral illumination also allow for more precise tomographic reconstructions [315]. It has also been demonstrated that confocal reconstructions are possible from tomographic acquisitions [127], delivering superior resolution images, albeit with intensity-only images, and not index of refraction images. Note that the precise measurement of resolution in coherent imaging requires some precautions [273,316]. Imaging of sample's fluctuations [264], apart from allowing to study intracellular dynamics, also permits to greatly improve resolution in tomographic imaging. Pump-probe approaches are also very promising [317], as temperature variations induce optical index variations, easily detected via the phase shift that the illumination beam then experiences [318].

On the opposite side of the scale, imaging of large samples also motivates numerous work in optical tomographic microscopy. Cell cultures, spheroids, animal models such as *C. elegans* worm or Zebrafish present specific difficulties because of their size and internal structures, inducing large phase retardation as well as multiple scattering properties. Single pixel detection has also been adapted to image millimeter-scale samples [102,172,280,304]. When the sample is too thick and/or too much scattering, or exhibits a very high absorbance, coherence is lost, and one enters in the diffuse imaging domain, or simply no light emerges from the specimen. For such samples, tomography in reflection (epi-tomography) can however still deliver useful information. Promising results have already been obtained, see [319,320] and references therein, and should motivate further developments, as for example speckle diffraction tomography [321].

Table 1 briefly recalls main characteristics of this imaging technique, as well as some challenges it presently faces in order to improve performances, as well as to experience a wider adoption by the end users.

Table 1. Main characteristics of tomographic microscopy and present challenges.

	Field of view	**Lateral resolution**	**Longitudinal resolution**	**Acquisition speed**	**Refractive index sensitivity**	**Cost**
Present situation	From about 100x100 μm at high resolution to millimeter size sample [231,280,322]	Sub 100 nm lateral resolution demonstrated [32,37]	Usually 2-3 times lower than lateral resolution. Isotropic resolution of about 180 nm demonstrated [37]	From a few seconds (e.g. rotating arm scanning [38,86]) to camera-speed limited only [193]	$\Delta n = 10^{-2}$ commonly obtained, even on biological samples, up to $\Delta n = 4.21\ 10^{-5}$ in large plastic samples [231]	From a few 100€ (lensless tomography) to about 50-70k€ (estimated) for a high-end 4Pi system (salaries and computers not included)
Challenges	Keeping high resolution in large volumes as in light-sheet microscopy	Development of nanometric superresolution for unlabeled samples [311,312]	Isotropic resolution using standard configurations	High resolution with rapid acquisitions compatibility. Combination with other microscopy techniques [323]	Development and adoption of metrological approaches [273,282–284]	Development of open-source alternatives, such as the OpenSPIM initiative [324]

7. Conclusion

TDM is known to deliver high quality 3D refractive index images of transparent or weakly absorbing samples, mainly encountered in biological imaging, in which many applications have already been developed. But the technique is not limited to this field, and finds applications in material sciences, surface characterization, etc ... However, one of the main limitations of TDM, compared for example to fluorescence microscopy, or Coherent Anti-Stocks Raman Scattering (CARS) microscopy, is a lack of selectivity in the reconstructed images. As a matter of fact, several types of sample structures can exhibit the exact same refractive index. Therefore, bringing back selectivity to TDM images is of tremendous importance. For this purpose, several research groups are exploiting the vectorial nature of light for

both acquisitions and reconstruction algorithms, in order exploit sensitivity to sample polarizability. This adds the possibility for TDM to characterize sample birefringence, and to extract polarization information such as local retardance, polarization orientation in 3D. If chemical selectivity is sought, exploiting absorption information brought by TDM is of great help. Despite being often neglected, wavelength dependence of the sample's absorption can be beneficially used to help distinguishing several chemical species. Therefore, coupling between TDM and hyperspectral imaging has also been considered. Properly coupled with polarization, it could probably exhibit an even greater selectivity.

One can also focus on data reconstruction. Knowledge of the detailed image formation model of conventional microscopes coupled with tomographic reconstruction makes it possible to perform multimodal reconstructions of investigated samples. However, computational work is, up to know, still considered with either first Born approximation, or Rytov approximation as an image formation model. This intrinsically limits the capabilities of TDM to tackle with imaging of multiple scattering thick samples, and strong refractive index variations. For this purpose, model relying on multi-layer approaches, coupled dipole resolution of Maxwell equations, or Born series approximation of Maxwell equations have been considered. Moreover, coupled with an adequate reconstruction formalism or inverse approaches, these reconstruction method are able to bring a solution to the "missing frequency" areas that are commonly occurring in 3D aperture synthesis.

The thrilling development this field has experienced in the last 20 years [8,63–68,283,286,287] was allowed by the spectacular progress in terms of speed, sensitivity, and decreasing costs of lasers, cameras and computers. This review also identifies future tracks to be explored, and hot topics to be addressed. Those certainly leave TDM development prone to a bright future, including the new capabilities brought in by deep-learning approaches, being it for hologram denoising, phase maps computations, sample reconstructions, or specimen analysis [188,222–225,325–335]

Author Contributions: N.V, O.H, and M.D all contributed to the article redaction. O.H. is the PI of the research team. M. D., and N. V. built the instrument, and processing software.

Funding: This research was funded by Région Grand-Est grant numbers FRCR 18P-07855, and FRCR 19P-10656, and by Agence Nationale de la Recherche grant numbers ANR-18-CE45-0010, ANR-19-CE42-0004, and ANR-22-CE42-0004. The APC was fully waived by MDPI.

Data Availability Statement: Data underlying the results presented in this paper are not publicly available at this time but may be obtained from the authors upon reasonable request.

Acknowledgments: The authors would like to thank the three anonymous reviewers for their valuable suggestions to improve the manuscript.

Conflicts of Interest: The authors declare no conflict of interest.

References

1. Hell, S.W.; Wichmann, J. Breaking the diffraction resolution limit by stimulated emission: stimulated-emission-depletion fluorescence microscopy. *Opt. Lett.* **1994**, *19*, 780–782. https://doi.org/10.1364/OL.19.000780.
2. Betzig, E.; Patterson, G.H.; Sougrat, R.; Lindwasser, O.W.; Olenych, S.; Bonifacino, J.S.; Davidson, M.W.; Lippincott-Schwartz, J.; Hess, H.F. Imaging Intracellular Fluorescent Proteins at Nanometer Resolution. *Science* **2006**, *313*, 1642–1645. https://doi.org/10.1126/science.1127344.
3. Rust, M.J.; Bates, M.; Zhuang, X. Sub-diffraction-limit imaging by stochastic optical reconstruction microscopy (STORM). *Nature Methods* **2006**, *3*, 793–796. https://doi.org/10.1038/nmeth929.
4. Balzarotti, F.; Eilers, Y.; Gwosch, K.C.; Gynnå, A.H.; Westphal, V.; Stefani, F.D.; Elf, J.; Hell, S.W. Nanometer resolution imaging and tracking of fluorescent molecules with minimal photon fluxes. *Science* **2017**, *355*, 606–612. https://doi.org/10.1126/science.aak9913.
5. Icha, J.; Weber, M.; Waters, J.C.; Norden, C. Phototoxicity in live fluorescence microscopy, and how to avoid it. *BioEssays* **2017**, *39*, 1700003. https://doi.org/https://doi.org/10.1002/bies.201700003.
6. Kumari, A.; Kesarwani, S.; Javoor, M.G.; Vinothkumar, K.R.; Sirajuddin, M. Structural insights into actin filament recognition by commonly used cellular actin markers. *The EMBO Journal* **2020**, *39*, e104006. https://doi.org/https://doi.org/10.15252/embj.2019104006.
7. Pospich, S.; Merino, F.; Raunser, S. Structural Effects and Functional Implications of Phalloidin and Jasplakinolide Binding to Actin Filaments. *Structure* **2020**, *28*, 437–449.e5. https://doi.org/10.1016/j.str.2020.01.014.
8. Park, Y.; Depeursinge, C.; Popescu, G. Quantitative phase imaging in biomedicine. *Nature Photonics* **2018**, *12*, 578–589. https://doi.org/10.1038/s41566-018-0253-x.
9. Ou, X.; Horstmeyer, R.; Yang, C.; Zheng, G. Quantitative phase imaging via Fourier ptychographic microscopy. *Opt. Lett.* **2013**, *38*, 4845–4848. https://doi.org/10.1364/OL.38.004845.
10. Lee, K.; Park, Y. Quantitative phase imaging unit. *Opt. Lett.* **2014**, *39*, 3630–3633. https://doi.org/10.1364/OL.39.003630.

11. Bokemeyer, A.; Tepasse, P.R.; Quill, L.; Lenz, P.; Rijcken, E.; Vieth, M.; Ding, N.; Ketelhut, S.; Rieder, F.; Kemper, B.; et al. Quantitative Phase Imaging Using Digital Holographic Microscopy Reliably Assesses Morphology and Reflects Elastic Properties of Fibrotic Intestinal Tissue. *Scientific Reports* **2019**, *9*, 19388. https://doi.org/10.1038/s41598-019-56045-2.
12. Gabor, D. A new microscopic principle. *Nature* **1948**, *161*, 777–778. https://doi.org/https://doi.org/10.1038/161777a0.
13. Schnars, U.; Jüptner, W. Direct recording of holograms by a CCD target and numerical reconstruction. *Appl. Opt.* **1994**, *33*, 179–181. https://doi.org/https://doi.org/10.1364/AO.33.000179.
14. Schnars, U.; Jüptner, W.P.O. Digital recording and numerical reconstruction of holograms. *Meas. Sci. Technol.* **2002**, *13*, R85. https://doi.org/10.1088/0957-0233/13/9/201.
15. Verrier, N.; Atlan, M. Off-axis digital hologram reconstruction: some practical considerations. *Appl. Opt.* **2011**, *50*, H136–H146. https://doi.org/https://doi.org/10.1364/AO.50.00H136.
16. Verrier, N.; Alexandre, D.; Tessier, G.; Gross, M. Holographic microscopy reconstruction in both object and image half-spaces with an undistorted three-dimensional grid. *Appl. Opt.* **2015**, *54*, 4672–4677. https://doi.org/https://doi.org/10.1364/AO.54.004672.
17. Leith, E.; Upatnieks, J. Reconstructed wavefronts and communication theory. *J. Opt. Soc. Am.* **1962**, *52*, 1123–1128. https://doi.org/https://doi.org/10.1364/JOSA.52.001123.
18. Cuche, E.; Marquet, P.; Depeursinge, C. Spatial filtering for zero-order and twin-image elimination in digital off-axis holography. *Appl. Opt.* **2000**, *39*, 4070–4075. https://doi.org/https://doi.org/10.1364/AO.39.004070.
19. Yamaguchi, I.; Zhang, T. Phase-shifting digital holography. *Opt. Lett.* **1997**, *22*, 1268–1270. https://doi.org/https://doi.org/10.1364/OL.22.001268.
20. Verrier, N.; Donnarumma, D.; Tessier, G.; Gross, M. High numerical aperture holographic microscopy reconstruction with extended z range. *Appl. Opt.* **2015**, *54*, 9540–9547. https://doi.org/https://doi.org/10.1364/AO.54.009540.
21. Wolf, E. Three-dimensional structure determination of semi-transparent objects from holographic data. *Opt. Commun.* **1969**, *1*, 153–156. https://doi.org/https://doi.org/10.1016/0030-4018(69)90052-2.
22. Kawata, S.; Touki, Y.; Minami, S. Optical Microscopic Tomography. In Proceedings of the Inverse Optics II; Bates, R.H.; Devaney, A.J., Eds. International Society for Optics and Photonics, SPIE, 1985, Vol. 0558, pp. 15 – 20. https://doi.org/10.1117/12.949566.
23. Kawata, S.; Nakamura, O.; Minami, S. Optical microscope tomography. I. Support constraint. *J. Opt. Soc. Am. A* **1987**, *4*, 292–297. https://doi.org/10.1364/JOSAA.4.000292.
24. Nakamura, O.; Kawata, S.; Minami, S. Optical microscope tomography. II. Nonnegative constraint by a gradient-projection method. *J. Opt. Soc. Am. A* **1988**, *5*, 554–561. https://doi.org/10.1364/JOSAA.5.000554.
25. Lauer, V. New approach to optical diffraction tomography yielding a vector equation of diffraction tomography and a novel tomographic microscope. *J. Microsc.* **2002**, *205*, 165–176. https://doi.org/https://doi.org/10.1046/j.0022-2720.2001.00980.x.
26. Charrière, F.; Marian, A.; Montfort, F.; Kuehn, J.; Colomb, T.; Cuche, E.; Marquet, P.; Depeursinge, C. Cell refractive index tomography by digital holographic microscopy. *Opt. Lett.* **2006**, *31*, 178–180. https://doi.org/https://doi.org/10.1364/OL.31.000178.
27. Choi, W.; Fang-Yen, C.; Badizadegan, K.; Oh, S.; Lue, N.; Dasari, R.R.; Feld, M.S. Tomographic phase microscopy. *Nature Methods* **2007**, *4*, 717–719. https://doi.org/10.1038/nmeth1078.
28. Ralston, T.S.; Marks, D.L.; Scott Carney, P.; Boppart, S.A. Interferometric synthetic aperture microscopy. *Nature Physics* **2007**, *3*, 129–134. https://doi.org/10.1038/nphys514.
29. Davis, B.J.; Marks, D.L.; Ralston, T.S.; Carney, P.S.; Boppart, S.A. Interferometric Synthetic Aperture Microscopy: Computed Imaging for Scanned Coherent Microscopy. *Sensors* **2008**, *8*, 3903–3931. https://doi.org/10.3390/s8063903.
30. Debailleul, M.; Simon, B.; Georges, V.; Haeberlé, O.; Lauer, V. Holographic microscopy and diffractive microtomography of transparent samples. *Measurement Science and Technology* **2008**, *19*, 074009. https://doi.org/10.1088/0957-0233/19/7/074009.
31. Debailleul, M.; Georges, V.; Simon, B.; Morin, R.; Haeberlé, O. High-resolution three-dimensional tomographic diffractive microscopy of transparent inorganic and biological samples. *Opt. Lett.* **2009**, *34*, 79–81. https://doi.org/10.1364/OL.34.000079.
32. Cotte, Y.; Toy, F.; Jourdain, P.; Pavillon, N.; Boss, D.; Magistretti, P.; Marquet, P.; Depeursinge, C. Marker-free phase nanoscopy. *Nature Photonics* **2013**, *7*, 113–117. https://doi.org/10.1038/nphoton.2012.329.
33. Agard, D.A. Optical Sectioning Microscopy: Cellular Architecture in Three Dimensions. *Annual Review of Biophysics and Bioengineering* **1984**, *13*, 191–219. https://doi.org/10.1146/annurev.bb.13.060184.001203.
34. Vertu, S.; Delaunay, J.J.; Yamada, I.; Haeberlé, O. Diffraction microtomography with sample rotation: influence of a missing apple core in the recorded frequency space. *Central European Journal of Physics* **2009**, *7*, 22–31. https://doi.org/doi:10.2478/s11534-008-0154-6.
35. Vertu, S.; Flügge, J.; Delaunay, J.J.; Haeberlé, O. Improved and isotropic resolution in tomographic diffractive microscopy combining sample and illumination rotation. *Central European Journal of Physics* **2011**, *9*, 969–974. https://doi.org/10.2478/s11534-011-0018-3.
36. Vinoth, B.; Lai, X.J.; Lin, Y.C.; Tu, H.Y.; Cheng, C.J. Integrated dual-tomography for refractive index analysis of free-floating single living cell with isotropic superresolution. *Scientific Reports* **2018**, *8*, 5943. https://doi.org/10.1038/s41598-018-24408-w.
37. Simon, B.; Debailleul, M.; Houkal, M.; Ecoffet, C.; Bailleul, J.; Lambert, J.; Spangenberg, A.; Liu, H.; Soppera, O.; Haeberlé, O. Tomographic diffractive microscopy with isotropic resolution. *Optica* **2017**, *4*, 460–463. https://doi.org/10.1364/OPTICA.4.000460.
38. https://www.nanolive.ch/.

39. https://www.tomocube.com/.
40. https://phioptics.com/.
41. Dändliker, R.; Weiss, K. Reconstruction of the three-dimensional refractive index from scattered waves. *Optics communications* **1970**, *1*, 323–328.
42. Coupland, J.M.; Lobera, J. Holography, tomography and 3D microscopy as linear filtering operations. *Measurement Science and Technology* **2008**, *19*, 074012. https://doi.org/10.1088/0957-0233/19/7/074012.
43. McCutchen, C.W. Generalized Aperture and the Three-Dimensional Diffraction Image. *J. Opt. Soc. Am.* **1964**, *54*, 240–244. https://doi.org/10.1364/JOSA.54.000240.
44. Devaney, A.J. Inverse-scattering theory within the Rytov approximation. *Opt. Lett.* **1981**, *6*, 374–376. https://doi.org/10.1364/OL.6.000374.
45. Chen, B.; Stamnes, J.J. Validity of diffraction tomography based on the first Born and the first Rytov approximations. *Applied optics* **1998**, *37*, 2996–3006.
46. Sentenac, A.; Mertz, J. Unified description of three-dimensional optical diffraction microscopy: from transmission microscopy to optical coherence tomography: tutorial. *J. Opt. Soc. Am. A* **2018**, *35*, 748–754. https://doi.org/10.1364/JOSAA.35.000748.
47. Streibl, N. Three-dimensional imaging by a microscope. *J. Opt. Soc. Am. A* **1985**, *2*, 121–127. https://doi.org/10.1364/JOSAA.2.000121.
48. Stallinga, S.; Radmacher, N.; Delon, A.; Enderlein, J. Optimal transfer functions for bandwidth-limited imaging. *Phys. Rev. Res.* **2022**, *4*, 023003. https://doi.org/10.1103/PhysRevResearch.4.023003.
49. Lin, Y.C.; Cheng, C.J. Sectional imaging of spatially refractive index distribution using coaxial rotation digital holographic microtomography. *Journal of Optics* **2014**, *16*, 065401. https://doi.org/10.1088/2040-8978/16/6/065401.
50. Bachelot, R.; Ecoffet, C.; Deloeil, D.; Royer, P.; Lougnot, D.J. Integration of micrometer-sized polymer elements at the end of optical fibers by free-radical photopolymerization. *Appl. Opt.* **2001**, *40*, 5860–5871. https://doi.org/10.1364/AO.40.005860.
51. Kozacki, T.; Krajewski, R.; Kujawińska, M. Reconstruction of refractive-index distribution in off-axis digital holography optical diffraction tomographic system. *Opt. Express* **2009**, *17*, 13758–13767. https://doi.org/10.1364/OE.17.013758.
52. Kostencka, J.; Kozacki, T.; Kuś, A.; Kujawińska, M. Accurate approach to capillary-supported optical diffraction tomography. *Opt. Express* **2015**, *23*, 7908–7923. https://doi.org/10.1364/OE.23.007908.
53. Kim, K.; Yoon, J.; Park, Y. Simultaneous 3D visualization and position tracking of optically trapped particles using optical diffraction tomography. *Optica* **2015**, *2*, 343–346. https://doi.org/10.1364/OPTICA.2.000343.
54. Vouldis, A.T.; Kechribaris, C.N.; Maniatis, T.A.; Nikita, K.S.; Uzunoglu, N.K. Investigating the enhancement of three-dimensional diffraction tomography by using multiple illumination planes. *J. Opt. Soc. Am. A* **2005**, *22*, 1251–1262. https://doi.org/10.1364/JOSAA.22.001251.
55. Vouldis, A.T.; Kechribaris, C.N.; Maniatis, T.A.; Nikita, K.S.; Uzunoglu, N.K. Three-Dimensional Diffraction Tomography Using Filtered Backpropagation and Multiple Illumination Planes. *IEEE Transactions on Instrumentation and Measurement* **2006**, *55*, 1975–1984. https://doi.org/10.1109/TIM.2006.884276.
56. Vertu, S.; Ochiai, M.; Shuzo, M.; Yamada, I.; Delaunay, J.J.; Haeberlé, O.; Okamoto, Y. Optical projection microtomography of transparent objects. In Proceedings of the Optical Coherence Tomography and Coherence Techniques III. Optica Publishing Group, 2007, p. 6627.
57. Kühn, J.; Montfort, F.; Colomb, T.; Rappaz, B.; Moratal, C.; Pavillon, N.; Marquet, P.; Depeursinge, C. Submicrometer tomography of cells by multiple-wavelength digital holographic microscopy in reflection. *Opt. Lett.* **2009**, *34*, 653–655. https://doi.org/10.1364/OL.34.000653.
58. Kim, M.K. Wavelength-scanning digital interference holography for optical section imaging. *Opt. Lett.* **1999**, *24*, 1693–1695. https://doi.org/10.1364/OL.24.001693.
59. Kim, T.; Zhou, R.; Mir, M.; Babacan, S.D.; Carney, P.S.; Goddard, L.L.; Popescu, G. White-light diffraction tomography of unlabelled live cells. *Nature Photonics* **2014**, *8*, 256–263. https://doi.org/10.1038/nphoton.2013.350.
60. Wang, Z.; Millet, L.; Mir, M.; Ding, H.; Unarunotai, S.; Rogers, J.; Gillette, M.U.; Popescu, G. Spatial light interference microscopy (SLIM). *Opt. Express* **2011**, *19*, 1016–1026. https://doi.org/10.1364/OE.19.001016.
61. Wang, Z.; Marks, D.L.; Carney, P.S.; Millet, L.J.; Gillette, M.U.; Mihi, A.; Braun, P.V.; Shen, Z.; Prasanth, S.G.; Popescu, G. Spatial light interference tomography (SLIT). *Opt. Express* **2011**, *19*, 19907–19918. https://doi.org/10.1364/OE.19.019907.
62. Lee, M.; Kim, K.; Oh, J.; Park, Y. Isotropically resolved label-free tomographic imaging based on tomographic moulds for optical trapping. *Light: Science & Applications* **2021**, *10*, 102.
63. Haeberlé, O.; Belkebir, K.; Giovaninni, H.; Sentenac, A. Tomographic diffractive microscopy: basics, techniques and perspectives. *Journal of Modern Optics* **2010**, *57*, 686–699.
64. South, F.A.; Liu, Y.Z.; Carney, P.S.; Boppart, S.A. Computed Optical Interferometric Imaging: Methods, Achievements, and Challenges. *IEEE Journal of Selected Topics in Quantum Electronics* **2016**, *22*, 186–196. https://doi.org/10.1109/JSTQE.2015.2493962.
65. Jin, D.; Zhou, R.; Yaqoob, Z.; So, P.T.C. Tomographic phase microscopy: principles and applications in bioimaging [Invited]. *J. Opt. Soc. Am. B* **2017**, *34*, B64–B77. https://doi.org/10.1364/JOSAB.34.000B64.
66. Kuś, A.; Krauze, W.; Makowski, P.L.; Kujawińska, M. Holographic tomography: hardware and software solutions for 3D quantitative biomedical imaging (Invited paper). *ETRI Journal* **2019**, *41*, 61–72. https://doi.org/https://doi.org/10.4218/etrij.2018-0505.

67. Balasubramani, V.; Kuś, A.; Tu, H.Y.; Cheng, C.J.; Baczewska, M.; Krauze, W.; Kujawińska, M. Holographic tomography: techniques and biomedical applications [Invited]. *Appl. Opt.* **2021**, *60*, B65–B80. https://doi.org/10.1364/AO.416902.
68. Chen, X.; Kandel, M.E.; Popescu, G. Spatial light interference microscopy: principle and applications to biomedicine. *Adv. Opt. Photon.* **2021**, *13*, 353–425. https://doi.org/10.1364/AOP.417837.
69. Fournier, C.; Haeberle, O. In *Unconventional Optical Imaging for Biology*; ISTE-Wiley, 2024.
70. Kuś, A.; Dudek, M.; Kemper, B.; Kujawińska, M.; Vollmer, A. Tomographic phase microscopy of living three-dimensional cell cultures. *Journal of biomedical optics* **2014**, *19*, 046009–046009.
71. Fienup, J.R. Phase retrieval algorithms: a comparison. *Appl. Opt.* **1982**, *21*, 2758–2769. https://doi.org/10.1364/AO.21.002758.
72. Taddese, A.M.; Verrier, N.; Debailleul, M.; Courbot, J.B.; Haeberlé, O. Optimizing sample illumination scanning in transmission tomographic diffractive microscopy. *Appl. Opt.* **2021**, *60*, 1694–1704.
73. Taddese, A.M.; Lo, M.; Verrier, N.; Debailleul, M.; Haeberlé, O. Jones tomographic diffractive microscopy with a polarized array sensor. *Opt. Express* **2023**, *31*, 9034–9051. https://doi.org/10.1364/OE.483050.
74. Clerc, F.L.; Gross, M.; Collot, L. Synthetic-aperture experiment in the visible with on-axis digital heterodyne holography. *Opt. Lett.* **2001**, *26*, 1550–1552.
75. Vargas, J.; Quiroga, J.A.; Belenguer, T. Phase-shifting interferometry based on principal component analysis. *Opt. Lett.* **2011**, *36*, 1326–1328. https://doi.org/10.1364/OL.36.001326.
76. Vargas, J.; Wang, S.; Gómez-Pedrero, J.A.; Estrada, J.C. Robust weighted principal components analysis demodulation algorithm for phase-shifting interferometry. *Opt. Express* **2021**, *29*, 16534–16546. https://doi.org/10.1364/OE.416344.
77. Simon, B.; Debailleul, M.; Georges, V.; Lauer, V.; Haeberlé, O. Tomographic diffractive microscopy of transparent samples. *The European Physical Journal-Applied Physics* **2008**, *44*, 29–35.
78. Simon, B.; Debailleul, M.; Beghin, A.; Tourneur, Y.; Haeberlé, O. High-resolution tomographic diffractive microscopy of biological samples. *Journal of Biophotonics* **2010**, *3*, 462–467, [https://onlinelibrary.wiley.com/doi/pdf/10.1002/jbio.200900094]. https://doi.org/10.1002/jbio.200900094.
79. Liu, F.; Chen, C.H. Electrohydrodynamic cone-jet bridges: Stability diagram and operating modes. *Journal of Electrostatics* **2014**, *72*, 330–335. https://doi.org/https://doi.org/10.1016/j.elstat.2014.05.004.
80. Foucault, L.; Verrier, N.; Debailleul, M.; Courbot, J.B.; Colicchio, B.; Simon, B.; Vonna, L.; Haeberlé, O. Versatile transmission/reflection tomographic diffractive microscopy approach. *J. Opt. Soc. Am. A* **2019**, *36*, C18–C27.
81. Sung, Y.; Choi, W.; Lue, N.; Dasari, R.R.; Yaqoob, Z. Stain-free quantification of chromosomes in live cells using regularized tomographic phase microscopy. *PloS one* **2012**, *7*, e49502.
82. Kostencka, J.; Kozacki, T.; Kuś, A.; Kemper, B.; Kujawińska, M. Holographic tomography with scanning of illumination: space-domain reconstruction for spatially invariant accuracy. *Biomedical optics express* **2016**, *7*, 4086–4101.
83. Noda, T.; Kawata, S.; Minami, S. Three-dimensional phase-contrast imaging by a computed-tomography microscope. *Appl. Opt.* **1992**, *31*, 670–674. https://doi.org/10.1364/AO.31.000670.
84. Kim, M.; Choi, Y.; Fang-Yen, C.; Sung, Y.; Dasari, R.R.; Feld, M.S.; Choi, W. High-speed synthetic aperture microscopy for live cell imaging. *Opt. Lett.* **2011**, *36*, 148–150. https://doi.org/10.1364/OL.36.000148.
85. Berdeu, A.; Laperrousaz, B.; Bordy, T.; Mandula, O.; Morales, S.; Gidrol, X.; Picollet-D'hahan, N.; Allier, C. Lens-free microscopy for 3D+ time acquisitions of 3D cell culture. *Scientific reports* **2018**, *8*, 16135.
86. Zdańkowski, P.; Winnik, J.; Patorski, K.; Gocłowski, P.; Ziemczonok, M.; Józwik, M.; Kujawińska, M.; Trusiak, M. Common-path intrinsically achromatic optical diffraction tomography. *Biomed. Opt. Express* **2021**, *12*, 4219–4234. https://doi.org/10.1364/BOE.428828.
87. Kou, S.S.; Sheppard, C.J.R. Image formation in holographic tomography: high-aperture imaging conditions. *Appl. Opt.* **2009**, *48*, H168–H175. https://doi.org/10.1364/AO.48.00H168.
88. Momey, F.; Berdeu, A.; Bordy, T.; Dinten, J.M.; Marcel, F.K.; Picollet-D'Hahan, N.; Gidrol, X.; Allier, C. Lensfree diffractive tomography for the imaging of 3D cell cultures. *Biomedical optics express* **2016**, *7*, 949–962.
89. Kuś, A.; Krauze, W.; Kujawińska, M. Active limited-angle tomographic phase microscope. *Journal of biomedical optics* **2015**, *20*, 111216–111216.
90. Chowdhury, S.; Eldridge, W.J.; Wax, A.; Izatt, J. Refractive index tomography with structured illumination. *Optica* **2017**, *4*, 537–545.
91. Balasubramani, V.; Tu, H.Y.; Lai, X.J.; Cheng, C.J. Adaptive wavefront correction structured illumination holographic tomography. *Scientific reports* **2019**, *9*, 10489.
92. Deng, Y.; Huang, C.H.; Vinoth, B.; Chu, D.; Lai, X.J.; Cheng, C.J. A compact synthetic aperture digital holographic microscope with mechanical movement-free beam scanning and optimized active aberration compensation for isotropic resolution enhancement. *Optics and Lasers in Engineering* **2020**, *134*, 106251.
93. Park, C.; Lee, K.; Baek, Y.; Park, Y. Low-coherence optical diffraction tomography using a ferroelectric liquid crystal spatial light modulator. *Opt. Express* **2020**, *28*, 39649–39659. https://doi.org/10.1364/OE.405418.
94. Nguyen, T.H.; Popescu, G. Spatial Light Interference Microscopy (SLIM) using twisted-nematic liquid-crystal modulation. *Biomed. Opt. Express* **2013**, *4*, 1571–1583. https://doi.org/10.1364/BOE.4.001571.
95. Shin, S.; Kim, K.; Yoon, J.; Park, Y. Active illumination using a digital micromirror device for quantitative phase imaging. *Opt. Lett.* **2015**, *40*, 5407–5410. https://doi.org/10.1364/OL.40.005407.

96. Shin, S.; Kim, K.; Kim, T.; Yoon, J.; Hong, K.; Park, J.; Park, Y. Optical diffraction tomography using a digital micromirror device for stable measurements of 4D refractive index tomography of cells. In Proceedings of the Quantitative Phase Imaging II. International Society for Optics and Photonics, 2016, Vol. 9718, p. 971814.
97. Lee, K.; Kim, K.; Kim, G.; Shin, S.; Park, Y. Time-multiplexed structured illumination using a DMD for optical diffraction tomography. *Opt. Lett.* **2017**, *42*, 999–1002. https://doi.org/10.1364/OL.42.000999.
98. Jin, D.; Zhou, R.; Yaqoob, Z.; So, P.T.C. Dynamic spatial filtering using a digital micromirror device for high-speed optical diffraction tomography. *Opt. Express* **2018**, *26*, 428–437. https://doi.org/10.1364/OE.26.000428.
99. Chowdhury, S.; Dhalla, A.H.; Izatt, J. Structured oblique illumination microscopy for enhanced resolution imaging of non-fluorescent, coherently scattering samples. *Biomed. Opt. Express* **2012**, *3*, 1841–1854. https://doi.org/10.1364/BOE.3.001841.
100. Liu, R.; Wen, K.; Li, J.; Ma, Y.; Zheng, J.; An, S.; Min, J.; Zalevsky, Z.; Yao, B.; Gao, P. Multi-harmonic structured illumination-based optical diffraction tomography. *Appl. Opt.* **2023**, *62*, 9199–9206. https://doi.org/10.1364/AO.508138.
101. Wicker, K.; Heintzmann, R. Resolving a misconception about structured illumination. *Nature Photonics* **2014**, *8*, 342–344.
102. Isikman, S.O.; Bishara, W.; Mavandadi, S.; Yu, F.W.; Feng, S.; Lau, R.; Ozcan, A. Lens-free optical tomographic microscope with a large imaging volume on a chip. *Proceedings of the National Academy of Sciences* **2011**, *108*, 7296–7301.
103. Horstmeyer, R.; Chung, J.; Ou, X.; Zheng, G.; Yang, C. Diffraction tomography with Fourier ptychography. *Optica* **2016**, *3*, 827–835. https://doi.org/10.1364/OPTICA.3.000827.
104. Gorski, W.; Osten, W. Tomographic imaging of photonic crystal fibers. *Optics letters* **2007**, *32*, 1977–9. https://doi.org/10.1364/OL.32.001977.
105. Dragomir, N.; Goh, X.M.; Roberts, A. Three-dimensional refractive index reconstruction with quantitative phase tomography. *Microscopy research and technique* **2008**, *71*, 5–10.
106. Kostencka, J.; Kozacki, T.; Józwik, M. Holographic tomography with object rotation and two-directional off-axis illumination. *Opt. Express* **2017**, *25*, 23920–23934. https://doi.org/10.1364/OE.25.023920.
107. WEDBERG, T.C.; WEDBERG, W.C. Tomographic reconstruction of the cross-sectional refractive index distribution in semi-transparent, birefringent fibres. *Journal of Microscopy* **1995**, *177*, 53–67, [https://onlinelibrary.wiley.com/doi/pdf/10.1111/j.1365-2818.1995.tb03533.x]. https://doi.org/https://doi.org/10.1111/j.1365-2818.1995.tb03533.x.
108. Malek, M.; Khelfa, H.; Picart, P.; Mounier, D.; Poilâne, C. Microtomography imaging of an isolated plant fiber: a digital holographic approach. *Appl. Opt.* **2016**, *55*, A111–A121. https://doi.org/10.1364/AO.55.00A111.
109. Lue, N.; Choi, W.; Popescu, G.; Badizadegan, K.; Dasari, R.R.; Feld, M.S. Synthetic aperture tomographic phase microscopy for 3D imaging of live cells in translational motion. *Opt. Express* **2008**, *16*, 16240–16246. https://doi.org/10.1364/OE.16.016240.
110. Ashkin, A.; Dziedzic, J.M.; Bjorkholm, J.E.; Chu, S. Observation of a single-beam gradient force optical trap for dielectric particles. *Opt. Lett.* **1986**, *11*, 288–290. https://doi.org/10.1364/OL.11.000288.
111. Habaza, M.; Gilboa, B.; Roichman, Y.; Shaked, N.T. Tomographic phase microscopy with 180° rotation of live cells in suspension by holographic optical tweezers. *Opt. Lett.* **2015**, *40*, 1881–1884. https://doi.org/10.1364/OL.40.001881.
112. chih Lin, Y.; Chen, H.C.; Tu, H.Y.; Liu, C.Y.; Cheng, C.J. Optically driven full-angle sample rotation for tomographic imaging in digital holographic microscopy. *Opt. Lett.* **2017**, *42*, 1321–1324. https://doi.org/10.1364/OL.42.001321.
113. Kim, K.; Park, Y. Tomographic active optical trapping of arbitrarily shaped objects by exploiting 3D refractive index maps. *Nature communications* **2017**, *8*, 15340.
114. Kreysing, M.K.; Kießling, T.; Fritsch, A.; Dietrich, C.; Guck, J.R.; Käs, J.A. The optical cell rotator. *Opt. Express* **2008**, *16*, 16984–16992. https://doi.org/10.1364/OE.16.016984.
115. Sun, J.; Yang, B.; Koukourakis, N.; Guck, J.; Czarske, J.W. AI-driven projection tomography with multicore fibre-optic cell rotation. *Nature Communications* **2024**, *15*, 147.
116. Jones, T.B. Basic theory of dielectrophoresis and electrorotation. *IEEE Engineering in medicine and Biology Magazine* **2003**, *22*, 33–42.
117. Kelbauskas, L.; Shetty, R.; Cao, B.; Wang, K.C.; Smith, D.; Wang, H.; Chao, S.H.; Gangaraju, S.; Ashcroft, B.; Kritzer, M.; et al. Optical computed tomography for spatially isotropic four-dimensional imaging of live single cells. *Science advances* **2017**, *3*, e1602580.
118. Habaza, M.; Kirschbaum, M.; Guernth-Marschner, C.; Dardikman, G.; Barnea, I.; Korenstein, R.; Duschl, C.; Shaked, N.T. Rapid 3D refractive-index imaging of live cells in suspension without labeling using dielectrophoretic cell rotation. *Advanced Science* **2017**, *4*, 1600205.
119. Ahmed, D.; Ozcelik, A.; Bojanala, N.; Nama, N.; Upadhyay, A.; Chen, Y.; Hanna-Rose, W.; Huang, T.J. Rotational manipulation of single cells and organisms using acoustic waves. *Nature communications* **2016**, *7*, 11085.
120. Cacace, T.; Memmolo, P.; Villone, M.M.; De Corato, M.; Mugnano, M.; Paturzo, M.; Ferraro, P.; Maffettone, P.L. Assembling and rotating erythrocyte aggregates by acoustofluidic pressure enabling full phase-contrast tomography. *Lab Chip* **2019**, *19*, 3123–3132. https://doi.org/10.1039/C9LC00629J.
121. Abbessi, R.; Verrier, N.; Taddese, A.M.; Laroche, S.; Debailleul, M.; Lo, M.; Courbot, J.B.; Haeberlé, O. Multimodal image reconstruction from tomographic diffraction microscopy data. *J. Microsc.* **2022**, *288*, 193–206.
122. Samson, E.C.; Blanca, C.M. Dynamic contrast enhancement in widefield microscopy using projector-generated illumination patterns. *New Journal of Physics* **2007**, *9*, 363.
123. Fan, X.; Healy, J.J.; O'Dwyer, K.; Hennelly, B.M. Label-free color staining of quantitative phase images of biological cells by simulated Rheinberg illumination. *Appl. Opt.* **2019**, *58*, 3104–3114.

124. Vishnyakov, G.; Levin, G.; Minaev, V.; Latushko, M.; Nekrasov, N.; Pickalov, V. Differential interference contrast tomography. *Opt. Lett.* **2016**, *41*, 3037–3040.
125. Bailleul, J.; Simon, B.; Debailleul, M.; Haeberlé, O., An Introduction to Tomographic Diffractive Microscopy. In *Micro- and Nanophotonic Technologies*; John Wiley and Sons, Ltd, 2017; chapter 18, pp. 425–442. https://doi.org/https://doi.org/10.1002/9783527699940.ch18.
126. Chang, T.; Shin, S.; Lee, M.; Park, Y. Computational approach to dark-field optical diffraction tomography. *Apl Photonics* **2020**, *5*.
127. Rasedujjaman, M.; Affannoukoué, K.; Garcia-Seyda, N.; Robert, P.; Giovannini, H.; Chaumet, P.C.; Theodoly, O.; Valignat, M.P.; Belkebir, K.; Sentenac, A.; et al. Three-dimensional imaging with reflection synthetic confocal microscopy. *Opt. Lett.* **2020**, *45*, 3721–3724. https://doi.org/10.1364/OL.397364.
128. von F. Zernike. Beugungstheorie des schneidenver-fahrens und seiner verbesserten form, der phasenkontrastmethode. *Physica* **1934**, *1*, 689–704.
129. https://github.com/madeba/MTD_transmission/blob/master/Python_Tomo/PretraitementMulti.py.
130. Ralston, T.S.; Marks, D.L.; Carney, P.S.; Boppart, S.A. Real-time interferometric synthetic aperture microscopy. *Opt. Express* **2008**, *16*, 2555–2569. https://doi.org/10.1364/OE.16.002555.
131. Bailleul, J.; Simon, B.; Debailleul, M.; Liu, H.; Haeberlé, O. GPU acceleration towards real-time image reconstruction in 3D tomographic diffractive microscopy. In Proceedings of the Real-Time Image and Video Processing 2012. SPIE, 2012, Vol. 8437, pp. 65–79.
132. Kim, K.; Kim, K.S.; Park, H.; Ye, J.C.; Park, Y. Real-time visualization of 3-D dynamic microscopic objects using optical diffraction tomography. *Optics express* **2013**, *21*, 32269–32278.
133. Ahmad, A.; Shemonski, N.D.; Adie, S.G.; Kim, H.S.; Hwu, W.M.W.; Carney, P.S.; Boppart, S.A. Real-time in vivo computed optical interferometric tomography. *Nature Photonics* **2013**, *7*, 444–448. https://doi.org/10.1038/nphoton.2013.71.
134. Backoach, O.; Kariv, S.; Girshovitz, P.; Shaked, N.T. Fast phase processing in off-axis holography by CUDA including parallel phase unwrapping. *Opt. Express* **2016**, *24*, 3177–3188. https://doi.org/10.1364/OE.24.003177.
135. Bailleul, J.; Simon, B.; Debailleul, M.; Foucault, L.; Verrier, N.; Haeberlé, O. Tomographic diffractive microscopy: Towards high-resolution 3-D real-time data acquisition, image reconstruction and display of unlabeled samples. *Opt. Commun.* **2018**, *422*, 28 – 37.
136. Yasuhiko, O.; Takeuchi, K.; Yamada, H.; Ueda, Y. Multiple-scattering suppressive refractive index tomography for the label-free quantitative assessment of multicellular spheroids. *Biomed. Opt. Express* **2022**, *13*, 962–979. https://doi.org/10.1364/BOE.446622.
137. Yasuhiko, O.; Takeuchi, K. In-silico clearing approach for deep refractive index tomography by partial reconstruction and wave-backpropagation. *Light: Science & Applications* **2023**, *12*, 101.
138. Richardson, D.S.; Lichtman, J.W. Clarifying tissue clearing. *Cell* **2015**, *162*, 246–257.
139. Simonetti, F. Multiple scattering: The key to unravel the subwavelength world from the far-field pattern of a scattered wave. *Phys. Rev. E* **2006**, *73*, 036619. https://doi.org/10.1103/PhysRevE.73.036619.
140. Chen, F.C.; Chew, W.C. Experimental verification of super resolution in nonlinear inverse scattering. *Applied Physics Letters* **1998**, *72*, 3080–3082, [https://pubs.aip.org/aip/apl/article-pdf/72/23/3080/10176438/3080_1_online.pdf]. https://doi.org/10.1063/1.121547.
141. Sentenac, A.; Guérin, C.A.; Chaumet, P.C.; Drsek, F.; Giovannini, H.; Bertaux, N.; Holschneider, M. Influence of multiple scattering on the resolution of an imaging system: a Cramér-Rao analysis. *Opt. Express* **2007**, *15*, 1340–1347. https://doi.org/10.1364/OE.15.001340.
142. Kamilov, U.S.; Papadopoulos, I.N.; Shoreh, M.H.; Goy, A.; Vonesch, C.; Unser, M.; Psaltis, D. Optical Tomographic Image Reconstruction Based on Beam Propagation and Sparse Regularization. *IEEE Transactions on Computational Imaging* **2016**, *2*, 59–70. https://doi.org/10.1109/TCI.2016.2519261.
143. Nesterov, Y. *Introductory lectures on convex optimization: A basic course*; Vol. 87, Springer Science & Business Media, 2013.
144. Chen, M.; Ren, D.; Liu, H.Y.; Chowdhury, S.; Waller, L. Multi-layer Born multiple-scattering model for 3D phase microscopy. *Optica* **2020**, *7*, 394–403.
145. Chowdhury, S.; Chen, M.; Eckert, R.; Ren, D.; Wu, F.; Repina, N.; Waller, L. High-resolution 3D refractive index microscopy of multiple-scattering samples from intensity images. *Optica* **2019**, *6*, 1211–1219.
146. Lee, M.; Hugonnet, H.; Park, Y. Inverse problem solver for multiple light scattering using modified Born series. *Optica* **2022**, *9*, 177–182. https://doi.org/10.1364/OPTICA.446511.
147. Bertero, M.; Boccacci, P.; De Mol, C. *Introduction to inverse problems in imaging*; CRC press, 2021.
148. Unger, K.D.; Chaumet, P.C.; Maire, G.; Sentenac, A.; Belkebir, K. Versatile inversion tool for phaseless optical diffraction tomography. *J. Opt. Soc. Am. A* **2019**, *36*, C1–C8. https://doi.org/10.1364/JOSAA.36.0000C1.
149. Pham, T.A.; Soubies, E.; Goy, A.; Lim, J.; Soulez, F.; Psaltis, D.; Unser, M. Versatile reconstruction framework for diffraction tomography with intensity measurements and multiple scattering. *Optics express* **2018**, *26*, 2749–2763.
150. Saba, A.; Lim, J.; Ayoub, A.B.; Antoine, E.E.; Psaltis, D. Polarization-sensitive optical diffraction tomography. *Optica* **2021**, *8*, 402–408.
151. Müller, P.; Schürmann, M.; Guck, J. ODTbrain: a Python library for full-view, dense diffraction tomography. *BMC bioinformatics* **2015**, *16*, 1–9.

152. Belkebir, K.; Chaumet, P.C.; Sentenac, A. Superresolution in total internal reflection tomography. *J. Opt. Soc. Am. A* **2005**, *22*, 1889–1897. https://doi.org/10.1364/JOSAA.22.001889.
153. Maire, G.; Drsek, F.; Girard, J.; Giovannini, H.; Talneau, A.; Konan, D.; Belkebir, K.; Chaumet, P.C.; Sentenac, A. Experimental demonstration of quantitative imaging beyond Abbe's limit with optical diffraction tomography. *Physical review letters* **2009**, *102*, 213905.
154. Feit, M.D.; Fleck, J.A. Light propagation in graded-index optical fibers. *Appl. Opt.* **1978**, *17*, 3990–3998. https://doi.org/10.1364/AO.17.003990.
155. Feit, M.; Fleck, J. Beam nonparaxiality, filament formation, and beam breakup in the self-focusing of optical beams. *JOSA B* **1988**, *5*, 633–640.
156. Fan, S.; Smith-Dryden, S.; Li, G.; Saleh, B. Iterative optical diffraction tomography for illumination scanning configuration. *Optics Express* **2020**, *28*, 39904–39915.
157. Denneulin, L.; Momey, F.; Brault, D.; Debailleul, M.; Taddese, A.M.; Verrier, N.; Haeberlé, O. GSURE criterion for unsupervised regularized reconstruction in tomographic diffractive microscopy. *J. Opt. Soc. Am. A* **2022**, *39*, A52–A61. https://doi.org/10.1364/JOSAA.444890.
158. Ma, X.; Xiao, W.; Pan, F. Optical tomographic reconstruction based on multi-slice wave propagation method. *Opt. Express* **2017**, *25*, 22595–22607. https://doi.org/10.1364/OE.25.022595.
159. Suski, D.; Winnik, J.; Kozacki, T. Fast multiple-scattering holographic tomography based on the wave propagation method. *Applied Optics* **2020**, *59*, 1397–1403.
160. Moser, S.; Jesacher, A.; Ritsch-Marte, M. Efficient and accurate intensity diffraction tomography of multiple-scattering samples. *Optics Express* **2023**, *31*, 18274–18289.
161. Brenner, K.H.; Singer, W. Light propagation through microlenses: a new simulation method. *Appl. Opt.* **1993**, *32*, 4984–4988. https://doi.org/10.1364/AO.32.004984.
162. Bao, Y.; Gaylord, T.K. Clarification and unification of the obliquity factor in diffraction and scattering theories: discussion. *JOSA A* **2017**, *34*, 1738–1745.
163. Tong, Z.; Ren, X.; Zhang, Z.; Wang, B.; Miao, Y.; Meng, G. Three-dimensional refractive index microscopy based on the multi-layer propagation model with obliquity factor correction. *Optics and Lasers in Engineering* **2024**, *174*, 107966. https://doi.org/https://doi.org/10.1016/j.optlaseng.2023.107966.
164. Goodman, J.W. *Introduction to Fourier optics*; Roberts and Company Publishers, 2005.
165. Liu, H.Y.; Liu, D.; Mansour, H.; Boufounos, P.T.; Waller, L.; Kamilov, U.S. SEAGLE: Sparsity-driven image reconstruction under multiple scattering. *IEEE Transactions on Computational Imaging* **2017**, *4*, 73–86.
166. Pham, T.a.; Soubies, E.; Ayoub, A.; Lim, J.; Psaltis, D.; Unser, M. Three-Dimensional Optical Diffraction Tomography With Lippmann-Schwinger Model. *IEEE Transactions on Computational Imaging* **2020**, *6*, 727–738. https://doi.org/10.1109/TCI.2020.2969070.
167. Born, M.; Wolf, E. *Principles of optics: electromagnetic theory of propagation, interference and diffraction of light*; Cambridge University, Cambridge, 1999.
168. Kamilov, U.S.; Liu, D.; Mansour, H.; Boufounos, P.T. A Recursive Born Approach to Nonlinear Inverse Scattering. *IEEE Signal Processing Letters* **2016**, *23*, 1052–1056. https://doi.org/10.1109/LSP.2016.2579647.
169. Osnabrugge, G.; Leedumrongwatthanakun, S.; Vellekoop, I.M. A convergent Born series for solving the inhomogeneous Helmholtz equation in arbitrarily large media. *Journal of Computational Physics* **2016**, *322*, 113–124. https://doi.org/https://doi.org/10.1016/j.jcp.2016.06.034.
170. Krüger, B.; Brenner, T.; Kienle, A. Solution of the inhomogeneous Maxwell's equations using a Born series. *Opt. Express* **2017**, *25*, 25165–25182. https://doi.org/10.1364/OE.25.025165.
171. Ciattoni, A.; Porto, P.D.; Crosignani, B.; Yariv, A. Vectorial nonparaxial propagation equation in the presence of a tensorial refractive-index perturbation. *J. Opt. Soc. Am. B* **2000**, *17*, 809–819. https://doi.org/10.1364/JOSAB.17.000809.
172. van Rooij, J.; Kalkman, J. Large-scale high-sensitivity optical diffraction tomography of zebrafish. *Biomed. Opt. Express* **2019**, *10*, 1782–1793. https://doi.org/10.1364/BOE.10.001782.
173. van Rooij, J.; Kalkman, J. Polarization contrast optical diffraction tomography. *Biomed. Opt. Express* **2020**, *11*, 2109–2121. https://doi.org/10.1364/BOE.381992.
174. South, F.A.; Liu, Y.Z.; Xu, Y.; Shemonski, N.D.; Carney, P.S.; Boppart, S.A. Polarization-sensitive interferometric synthetic aperture microscopy. *Applied Physics Letters* **2015**, *107*, 211106, [https://pubs.aip.org/aip/apl/article-pdf/doi/10.1063/1.4936236/13464566/211106_1_online.pdf]. https://doi.org/10.1063/1.4936236.
175. Park, K.; Yang, T.D.; Seo, D.; Hyeon, M.G.; Kong, T.; Kim, B.M.; Choi, Y.; Choi, W.; Choi, Y. Jones matrix microscopy for living eukaryotic cells. *ACS Photonics* **2021**, *8*, 3042–3050.
176. Shin, S.; Eun, J.; Lee, S.S.; Lee, C.; Hugonnet, H.; Yoon, D.K.; Kim, S.H.; Jeong, J.; Park, Y. Tomographic measurement of dielectric tensors at optical frequency. *Nature Materials* **2022**, *21*, 317–324. https://doi.org/10.1038/s41563-022-01202-8.
177. Mihoubi, S.; Lapray, P.J.; Bigué, L. Survey of Demosaicking Methods for Polarization Filter Array Images. *Sensors* **2018**, *18*. https://doi.org/10.3390/s18113688.
178. Verrier, N.; Taddese, A.M.; Abbessi, R.; Debailleul, M.; Haeberlé, O. 3D differential interference contrast microscopy using polarisation-sensitive tomographic diffraction microscopy. *J. Microsc.* **2023**, *289*, 128–133.

179. Sánchez-Ortiga, E.; Doblas, A.; Saavedra, G.; Martinez-Corral, M.; Garcia-Sucerquia, J. Off-axis digital holographic microscopy: Practical design parameters for operating at diffraction limit. *Applied optics* **2014**, *53*, 2058–2066. https://doi.org/10.1364/AO.53.002058.
180. Sung, Y.; Choi, W.; Fang-Yen, C.; Badizadegan, K.; Dasari, R.R.; Feld, M.S. Optical diffraction tomography for high resolution live cell imaging. *Optics Express* **2009**, *17*, 266–277.
181. Fiolka, R.; Wicker, K.; Heintzmann, R.; Stemmer, A. Simplified approach to diffraction tomography in optical microscopy. *Opt. Express* **2009**, *17*, 12407–12417. https://doi.org/10.1364/OE.17.012407.
182. Lim, J.; Lee, K.; Jin, K.H.; Shin, S.; Lee, S.; Park, Y.; Ye, J.C. Comparative study of iterative reconstruction algorithms for missing cone problems in optical diffraction tomography. *Optics Express* **2015**, *23*, 16933–16948.
183. Taddese, A.M.; Verrier, N.; Debailleul, M.; Courbot, J.B.; Haeberlé, O. Optimizing sample illumination scanning for reflection and 4Pi tomographic diffractive microscopy. *Appl. Opt.* **2021**, *60*, 7745–7753.
184. Aziz, J.A.B.; Smith-Dryden, S.; Saleh, B.E.A.; Li, G. Selection of Illumination Angles for Object Rotation and Illumination Scanning Configurations in Optical Diffraction Tomography. In Proceedings of the 2023 IEEE Photonics Conference (IPC), 2023, pp. 1–2. https://doi.org/10.1109/IPC57732.2023.10360673.
185. Aziz, J.A.B.; Smith-Dryden, S.; Li, G.; Saleh, B.E.A. Voronoi Weighting for Optical Diffraction Tomography using Nonuniform Illumination Angles. In Proceedings of the 2023 IEEE Photonics Conference (IPC), 2023, pp. 1–2. https://doi.org/10.1109/IPC57732.2023.10360744.
186. Liu, H.; Bailleul, J.; Simon, B.; Debailleul, M.; Colicchio, B.; Haeberlé, O. Tomographic diffractive microscopy and multiview profilometry with flexible aberration correction. *Appl. Opt.* **2014**, *53*, 748–755. https://doi.org/10.1364/AO.53.000748.
187. Machnio, P.; Ziemczonok, M.; Kujawińska, M. Reconstruction enhancement via projection screening in holographic tomography. *Photonics Letters of Poland* **2021**, *13*, 37–39. https://doi.org/10.4302/plp.v13i2.1104.
188. Ryu, D.; Jo, Y.; Yoo, J.; Chang, T.; Ahn, D.; Kim, Y.S.; Kim, G.; Min, H.S.; Park, Y. Deep learning-based optical field screening for robust optical diffraction tomography. *Scientific reports* **2019**, *9*, 15239.
189. Girshovitz, P.; Shaked, N.T. Real-time quantitative phase reconstruction in off-axis digital holography using multiplexing. *Opt. Lett.* **2014**, *39*, 2262–2265. https://doi.org/10.1364/OL.39.002262.
190. Rubin, M.; Dardikman, G.; Mirsky, S.K.; Turko, N.A.; Shaked, N.T. Six-pack off-axis holography. *Opt. Lett.* **2017**, *42*, 4611–4614. https://doi.org/10.1364/OL.42.004611.
191. Mirsky, S.K.; Barnea, I.; Shaked, N.T. Dynamic Tomographic Phase Microscopy by Double Six-Pack Holography. *ACS Photonics* **2022**, *9*, 1295–1303, [https://doi.org/10.1021/acsphotonics.1c01804]. https://doi.org/10.1021/acsphotonics.1c01804.
192. Foucault, L.; Verrier, N.; Debailleul, M.; Simon, B.; Haeberlé, O. Simplified tomographic diffractive microscopy for axisymmetric samples. *OSA Continuum* **2019**, *2*, 1039–1055.
193. Sung, Y. Snapshot Holographic Optical Tomography. *Physical Review Applied* **2019**, *11*, 014039.
194. Sung, Y. Snapshot Three-Dimensional Absorption Imaging of Microscopic Specimens. *Phys. Rev. Appl.* **2021**, *15*, 064065. https://doi.org/10.1103/PhysRevApplied.15.064065.
195. Kus, A. Real-time, multiplexed holographic tomography. *Optics and Lasers in Engineering* **2021**, *149*, 106783. https://doi.org/10.1016/j.optlaseng.2021.106783.
196. Wang, J.; Zhao, X.; Wang, Y.; Li, D. Quantitative real-time phase microscopy for extended depth-of-field imaging based on the 3D single-shot differential phase contrast (ssDPC) imaging method. *Opt. Express* **2024**, *32*, 2081–2096. https://doi.org/10.1364/OE.512285.
197. Zhang, J.; Dai, S.; Ma, C.; Xi, T.; Di, J.; Zhao, J. A review of common-path off-axis digital holography: towards high stable optical instrument manufacturing. *Light: advanced manufacturing* **2021**, *2*, 333–349.
198. Kim, Y.; Shim, H.; Kim, K.; Park, H.; Heo, J.H.; Yoon, J.; Choi, C.; Jang, S.; Park, Y. Common-path diffraction optical tomography for investigation of three-dimensional structures and dynamics of biological cells. *Opt. Express* **2014**, *22*, 10398–10407. https://doi.org/10.1364/OE.22.010398.
199. Bianchi, S.; Brasili, F.; Saglimbeni, F.; Cortese, B.; Leonardo, R.D. Optical diffraction tomography of 3D microstructures using a low coherence source. *Opt. Express* **2022**, *30*, 22321–22332. https://doi.org/10.1364/OE.454910.
200. Hsu, W.C.; Su, J.W.; Tseng, T.Y.; Sung, K.B. Tomographic diffractive microscopy of living cells based on a common-path configuration. *Opt. Lett.* **2014**, *39*, 2210–2213. https://doi.org/10.1364/OL.39.002210.
201. Kim, K.; Yaqoob, Z.; Lee, K.; Kang, J.W.; Choi, Y.; Hosseini, P.; So, P.T.C.; Park, Y. Diffraction optical tomography using a quantitative phase imaging unit. *Opt. Lett.* **2014**, *39*, 6935–6938. https://doi.org/10.1364/OL.39.006935.
202. Bon, P.; Maucort, G.; Wattellier, B.; Monneret, S. Quadriwave lateral shearing interferometry for quantitative phase microscopy of living cells. *Opt. Express* **2009**, *17*, 13080–13094. https://doi.org/10.1364/OE.17.013080.
203. Ruan, Y.; Bon, P.; Mudry, E.; Maire, G.; Chaumet, P.C.; Giovannini, H.; Belkebir, K.; Talneau, A.; Wattellier, B.; Monneret, S.; et al. Tomographic diffractive microscopy with a wavefront sensor. *Opt. Lett.* **2012**, *37*, 1631–1633. https://doi.org/10.1364/OL.37.001631.
204. Kak, A.C.; Slaney, M. *Principles of Computerized Tomographic Imaging*; Society for Industrial and Applied Mathematics, 2001; [https://epubs.siam.org/doi/pdf/10.1137/1.9780898719277]. https://doi.org/10.1137/1.9780898719277.
205. Maleki, M.H.; Devaney, A.J. Phase-retrieval and intensity-only reconstruction algorithms for optical diffraction tomography. *J. Opt. Soc. Am. A* **1993**, *10*, 1086–1092. https://doi.org/10.1364/JOSAA.10.001086.

206. Tian, L.; Waller, L. 3D intensity and phase imaging from light field measurements in an LED array microscope. *Optica* **2015**, *2*, 104–111. https://doi.org/10.1364/OPTICA.2.000104.
207. Soto, J.M.; Rodrigo, J.A.; Alieva, T. Label-free quantitative 3D tomographic imaging for partially coherent light microscopy. *Opt. Express* **2017**, *25*, 15699–15712. https://doi.org/10.1364/OE.25.015699.
208. Li, J.; Matlock, A.; Li, Y.; Chen, Q.; Tian, L.; Zuo, C. Resolution-enhanced intensity diffraction tomography in high numerical aperture label-free microscopy. *Photonics Research* **2020**, *8*, 1818–1826.
209. Ayoub, A.B.; Roy, A.; Psaltis, D. Optical Diffraction Tomography Using Nearly In-Line Holography with a Broadband LED Source. *Applied Sciences* **2022**, *12*. https://doi.org/10.3390/app12030951.
210. Ling, R.; Tahir, W.; Lin, H.Y.; Lee, H.; Tian, L. High-throughput intensity diffraction tomography with a computational microscope. *Biomedical optics express* **2018**, *9*, 2130–2141.
211. Matlock, A.; Tian, L. High-throughput, volumetric quantitative phase imaging with multiplexed intensity diffraction tomography. *Biomedical optics express* **2019**, *10*, 6432–6448.
212. Li, J.; Matlock, A.; Li, Y.; Chen, Q.; Zuo, C.; Tian, L. High-speed in vitro intensity diffraction tomography. *Advanced Photonics* **2019**, *1*, 066004–066004.
213. Li, J.; Chen, Q.; Zhang, J.; Zhang, Z.; Zhang, Y.; Zuo, C. Optical diffraction tomography microscopy with transport of intensity equation using a light-emitting diode array. *Optics and lasers in engineering* **2017**, *95*, 26–34.
214. Li, J.; Zhou, N.; Sun, J.; Zhou, S.; Bai, Z.; Lu, L.; Chen, Q.; Zuo, C. Transport of intensity diffraction tomography with non-interferometric synthetic aperture for three-dimensional label-free microscopy. *Light: Science & Applications* **2022**, *11*, 154.
215. Bai, Z.; Chen, Q.; Ullah, H.; Lu, L.; Zhou, N.; Zhou, S.; Li, J.; Zuo, C. Absorption and phase decoupling in transport of intensity diffraction tomography. *Optics and Lasers in Engineering* **2022**, *156*, 107082.
216. Ullah, H.; Li, J.; Zhou, S.; Bai, Z.; Ye, R.; Chen, Q.; Zuo, C. Parallel synthetic aperture transport-of-intensity diffraction tomography with annular illumination. *Optics Letters* **2023**, *48*, 1638–1641.
217. Zuo, C.; Li, J.; Sun, J.; Fan, Y.; Zhang, J.; Lu, L.; Zhang, R.; Wang, B.; Huang, L.; Chen, Q. Transport of intensity equation: a tutorial. *Optics and Lasers in Engineering* **2020**, *135*, 106187.
218. Shen, C.; Liang, M.; Pan, A.; Yang, C. Non-iterative complex wave-field reconstruction based on Kramers–Kronig relations. *Photonics Research* **2021**, *9*, 1003–1012.
219. Li, Y.; Huang, G.; Ma, S.; Wang, Y.; Liu, S.; Liu, Z. Single-frame two-color illumination computational imaging based on Kramers–Kronig relations. *Applied Physics Letters* **2023**, *123*.
220. Zhu, J.; Wang, H.; Tian, L. High-fidelity intensity diffraction tomography with a non-paraxial multiple-scattering model. *Optics Express* **2022**, *30*, 32808–32821.
221. Song, S.; Kim, J.; Moon, T.; Seong, B.; Kim, W.; Yoo, C.H.; Choi, J.K.; Joo, C. Polarization-sensitive intensity diffraction tomography. *Light: Science & Applications* **2023**, *12*, 124.
222. Wang, F.; Bian, Y.; Wang, H.; Lyu, M.; Pedrini, G.; Osten, W.; Barbastathis, G.; Situ, G. Phase imaging with an untrained neural network. *Light: Science & Applications* **2020**, *9*, 77.
223. Wang, K.; Song, L.; Wang, C.; Ren, Z.; Zhao, G.; Dou, J.; Di, J.; Barbastathis, G.; Zhou, R.; Zhao, J.; et al. On the use of deep learning for phase recovery. *Light: Science & Applications* **2024**, *13*, 4.
224. Matlock, A.; Zhu, J.; Tian, L. Multiple-scattering simulator-trained neural network for intensity diffraction tomography. *Optics Express* **2023**, *31*, 4094–4107.
225. Pierré, W.; Hervé, L.; Paviolo, C.; Mandula, O.; Remondiere, V.; Morales, S.; Grudinin, S.; Ray, P.F.; Dhellemmes, M.; Arnoult, C.; et al. 3D time-lapse imaging of a mouse embryo using intensity diffraction tomography embedded inside a deep learning framework. *Applied optics* **2022**, *61*, 3337–3348.
226. Soto, J.M.; Rodrigo, J.A.; Alieva, T. Optical diffraction tomography with fully and partially coherent illumination in high numerical aperture label-free microscopy [Invited]. *Appl. Opt.* **2018**, *57*, A205–A214. https://doi.org/10.1364/AO.57.00A205.
227. Soto, J.M.; Rodrigo, J.A.; Alieva, T. Partially coherent illumination engineering for enhanced refractive index tomography. *Opt. Lett.* **2018**, *43*, Soto20184699–4702. https://doi.org/10.1364/OL.43.004699.
228. Hugonnet, H.; Lee, M.; Park, Y. Optimizing illumination in three-dimensional deconvolution microscopy for accurate refractive index tomography. *Opt. Express* **2021**, *29*, 6293–6301. https://doi.org/10.1364/OE.412510.
229. Li, J.; Zhou, N.; Bai, Z.; Zhou, S.; Chen, Q.; Zuo, C. Optimization analysis of partially coherent illumination for refractive index tomographic microscopy. *Optics and Lasers in Engineering* **2021**, *143*, 106624. https://doi.org/https://doi.org/10.1016/j.optlaseng.2021.106624.
230. Cao, R.; Kellman, M.; Ren, D.; Eckert, R.; Waller, L. Self-calibrated 3D differential phase contrast microscopy with optimized illumination. *Biomed. Opt. Express* **2022**, *13*, 1671–1684. https://doi.org/10.1364/BOE.450838.
231. Luo, Z.; Yurt, A.; Stahl, R.; Carlon, M.S.; Ramalho, A.S.; Vermeulen, F.; Lambrechts, A.; Braeken, D.; Lagae, L. Fast compressive lens-free tomography for 3D biological cell culture imaging. *Opt. Express* **2020**, *28*, 26935–26952. https://doi.org/10.1364/OE.393492.
232. Merola, F.; Memmolo, P.; Miccio, L.; Savoia, R.; Mugnano, M.; Fontana, A.; d'Ippolito, G.; Sardo, A.; Iolascon, A.; Gambale, A.; et al. Tomographic flow cytometry by digital holography. *Light: Science & Applications* **2017**, *6*, e16241. https://doi.org/10.1038/lsa.2016.241.
233. Isikman, S.O.; Greenbaum, A.; Luo, W.; Coskun, A.F.; Ozcan, A. Giga-pixel lensfree holographic microscopy and tomography using color image sensors. *PLoS ONE* **2012**, *7*, e45044.

234. Villone, M.M.; Memmolo, P.; Merola, F.; Mugnano, M.; Miccio, L.; Maffettone, P.L.; Ferraro, P. Full-angle tomographic phase microscopy of flowing quasi-spherical cells. *Lab on a Chip* **2018**, *18*, 126–131.
235. Pirone, D.; Lim, J.; Merola, F.; Miccio, L.; Mugnano, M.; Bianco, V.; Cimmino, F.; Visconte, F.; Montella, A.; Capasso, M.; et al. Stain-free identification of cell nuclei using tomographic phase microscopy in flow cytometry. *Nature Photonics* **2022**, *16*, 1–9. https://doi.org/10.1038/s41566-022-01096-7.
236. Pirone, D.; Sirico, D.; Miccio, L.; Bianco, V.; Mugnano, M.; Giudice, D.; Pasquinelli, G.; Valente, S.; Lemma, S.; Iommarini, L.; et al. 3D imaging lipidometry in single cell by in-flow holographic tomography. *Opto-Electronic Advances* **2023**, *6*, 220048–220048. https://doi.org/10.29026/oea.2023.220048.
237. Bianco, V.; Massimo, D.; Pirone, D.; Giugliano, G.; Mosca, N.; Summa, M.; Scerra, G.; Memmolo, P.; Miccio, L.; Russo, T.; et al. Label-Free Intracellular Multi-Specificity in Yeast Cells by Phase-Contrast Tomographic Flow Cytometry. *Small methods* **2023**, *7*, e2300447. https://doi.org/10.1002/smtd.202300447.
238. Wang, Z.; Bianco, V.; Pirone, D.; Memmolo, P.; Villone, M.; Maffettone, P.L.; Ferraro, P. Dehydration of plant cells shoves nuclei rotation allowing for 3D phase-contrast tomography. *Light: Science & Applications* **2021**, *10*, 187. https://doi.org/10.1038/s41377-021-00626-2.
239. Pirone, D.; Memmolo, P.; Merola, F.; Miccio, L.; Mugnano, M.; Capozzoli, A.; Curcio, C.; Liseno, A.; Ferraro, P. Rolling angle recovery of flowing cells in holographic tomography exploiting the phase similarity. *Applied Optics* **2021**, *60*, A277. https://doi.org/10.1364/AO.404376.
240. Sung, Y. Hyperspectral Three-Dimensional Refractive-Index Imaging Using Snapshot Optical Tomography. *Phys. Rev. Appl.* **2023**, *19*, 014064. https://doi.org/10.1103/PhysRevApplied.19.014064.
241. Jung, J.; Kim, K.; Yoon, J.; Park, Y. Hyperspectral optical diffraction tomography. *Opt. Express* **2016**, *24*, 2006–2012. https://doi.org/10.1364/OE.24.002006.
242. Sung, Y. Spectroscopic Microtomography in the Visible Wavelength Range. *Phys. Rev. Applied* **2018**, *10*, 054041. https://doi.org/10.1103/PhysRevApplied.10.054041.
243. Juntunen, C.; Abramczyk, A.R.; Woller, I.M.; Sung, Y. Hyperspectral Three-Dimensional Absorption Imaging Using Snapshot Optical Tomography. *Phys. Rev. Appl.* **2022**, *18*, 034055. https://doi.org/10.1103/PhysRevApplied.18.034055.
244. Ossowski, P.; Kuś, A.; Krauze, W.; Tamborski, S.; Ziemczonok, M.; Kuźbicki, Ł.; Szkulmowski, M.; Kujawińska, M. Near-infrared, wavelength, and illumination scanning holographic tomography. *Biomed. Opt. Express* **2022**, *13*, 5971–5988. https://doi.org/10.1364/BOE.468046.
245. Juntunen, C.; Abramczyk, A.R.; Shea, P.; Sung, Y. Spectroscopic Microtomography in the Short-Wave Infrared Wavelength Range. *Sensors* **2023**, *23*. https://doi.org/10.3390/s23115164.
246. Tamamitsu, M.; Toda, K.; Shimada, H.; Honda, T.; Takarada, M.; Okabe, K.; Nagashima, Y.; Horisaki, R.; Ideguchi, T. Label-free biochemical quantitative phase imaging with mid-infrared photothermal effect. *Optica* **2020**, *7*, 359–366. https://doi.org/10.1364/OPTICA.390186.
247. Yurdakul, C.; Zong, H.; Bai, Y.; Cheng, J.X.; Ünlü, M.S. Bond-selective interferometric scattering microscopy. *Journal of Physics D: Applied Physics* **2021**, *54*, 364002. https://doi.org/10.1088/1361-6463/ac0b0d.
248. Zhang, D.; Lan, L.; Bai, Y.; Majeed, H.; Kandel, M.E.; Popescu, G.; Cheng, J.X. Bond-selective transient phase imaging via sensing of the infrared photothermal effect. *Light: Science & Applications* **2019**, *8*, 116.
249. Zhao, J.; Matlock, A.; Zhu, H.; Song, Z.; Zhu, J.; Wang, B.; Chen, F.; Zhan, Y.; Chen, Z.; Xu, Y.; et al. Bond-selective intensity diffraction tomography. *Nature Communications* **2022**, *13*, 7767.
250. Bai, Y.; Yin, J.; Cheng, J.X. Bond-selective imaging by optically sensing the mid-infrared photothermal effect. *Science Advances* **2021**, *7*, eabg1559, [https://www.science.org/doi/pdf/10.1126/sciadv.abg1559]. https://doi.org/10.1126/sciadv.abg1559.
251. Pu, Y.; Centurion, M.; Psaltis, D. Harmonic holography: a new holographic principle. *Appl. Opt.* **2008**, *47*, A103–A110. https://doi.org/10.1364/AO.47.00A103.
252. Shaffer, E.; Pavillon, N.; Kühn, J.; Depeursinge, C. Digital holographic microscopy investigation of second harmonic generated at a glass/air interface. *Opt. Lett.* **2009**, *34*, 2450–2452. https://doi.org/10.1364/OL.34.002450.
253. Shaffer, E.; Marquet, P.; Depeursinge, C. Real time, nanometric 3D-tracking of nanoparticles made possible by second harmonic generation digital holographic microscopy. *Optics Express* **2010**, *18*, 17392–17403.
254. Hsieh, C.L.; Grange, R.; Pu, Y.; Psaltis, D. Three-dimensional harmonic holographic microcopy using nanoparticles as probes for cell imaging. *Opt. Express* **2009**, *17*, 2880–2891. https://doi.org/10.1364/OE.17.002880.
255. Masihzadeh, O.; Schlup, P.; Bartels, R.A. Label-free second harmonic generation holographic microscopy of biological specimens. *Opt. Express* **2010**, *18*, 9840–9851. https://doi.org/10.1364/OE.18.009840.
256. Smith, D.R.; Winters, D.G.; Bartels, R.A. Submillisecond second harmonic holographic imaging of biological specimens in three dimensions. *Proceedings of the National Academy of Sciences* **2013**, *110*, 18391–18396.
257. Yu, W.; Li, X.; Hu, R.; Qu, J.; Liu, L. Full-field measurement of complex objects illuminated by an ultrashort pulse laser using delay-line sweeping off-axis interferometry. *Opt. Lett.* **2021**, *46*, 2803–2806. https://doi.org/10.1364/OL.421313.
258. Li, X.; Yu, W.; Hu, R.; Qu, J.; Liu, L. Fast polarization-sensitive second-harmonic generation microscopy based on off-axis interferometry. *Opt. Express* **2023**, *31*, 3143–3152. https://doi.org/10.1364/OE.471459.
259. Hu, C.; Field, J.J.; Kelkar, V.; Chiang, B.; Wernsing, K.; Toussaint, K.C.; Bartels, R.A.; Popescu, G. Harmonic optical tomography of nonlinear structures. *Nature Photonics* **2020**, *14*, 564–569.

260. Yu, W.; Li, X.; Wang, B.; Qu, J.; Liu, L. Optical diffraction tomography of second-order nonlinear structures in weak scattering media: theoretical analysis and experimental consideration. *Opt. Express* **2022**, *30*, 45724–45737. https://doi.org/10.1364/OE.472637.
261. Moon, J.; Kang, S.; Hong, J.H.; Yoon, S.; Choi, W. Synthetic aperture phase imaging of second harmonic generation field with computational adaptive optics. *arXiv preprint arXiv:2304.14018* **2023**.
262. Débarre, D.; Supatto, W.; Pena, A.M.; Fabre, A.; Tordjmann, T.; Combettes, L.; Schanne-Klein, M.C.; Beaurepaire, E. Imaging lipid bodies in cells and tissues using third-harmonic generation microscopy. *Nature methods* **2006**, *3*, 47–53.
263. Olivier, N.; Aptel, F.; Plamann, K.; Schanne-Klein, M.C.; Beaurepaire, E. Harmonic microscopy of isotropic and anisotropic microstructure of the human cornea. *Opt. Express* **2010**, *18*, 5028–5040. https://doi.org/10.1364/OE.18.005028.
264. Hugonnet, H.; Han, H.; Park, W.; Park, Y. Improving Specificity and Axial Spatial Resolution of Refractive Index Imaging by Exploiting Uncorrelated Subcellular Dynamics. *ACS Photonics* **2024**, *11*, 257–266. https://doi.org/10.1021/acsphotonics.3c01236.
265. Verrier, N.; Atlan, M. Absolute measurement of small-amplitude vibrations by time-averaged heterodyne holography with a dual local oscillator. *Opt. Lett.* **2013**, *38*, 739–741.
266. Verrier, N.; Alloul, L.; Gross, M. Vibration of low amplitude imaged in amplitude and phase by sideband versus carrier correlation digital holography. *Opt. Lett.* **2015**, *40*, 411–414.
267. Verrier, N.; Alexandre, D.; Gross, M. Laser Doppler holographic microscopy in transmission: application to fish embryo imaging. *Opt. Express* **2014**, *22*, 9368–9379.
268. Puyo, L.; Paques, M.; Fink, M.; Sahel, J.A.; Atlan, M. In vivo laser Doppler holography of the human retina. *Biomed. Opt. Express* **2018**, *9*, 4113–4129. https://doi.org/10.1364/BOE.9.004113.
269. Puyo, L.; Spahr, H.; Pfäffle, C.; Hüttmann, G.; Hillmann, D. Retinal blood flow imaging with combined full-field swept-source optical coherence tomography and laser Doppler holography. *Opt. Lett.* **2022**, *47*, 1198–1201. https://doi.org/10.1364/OL.449739.
270. Brodoline, A.; Rawat, N.; Alexandre, D.; Cubedo, N.; Gross, M. 4D compressive sensing holographic microscopy imaging of small moving objects. *Opt. Lett.* **2019**, *44*, 2827–2830.
271. Brodoline, A.; Rawat, N.; Alexandre, D.; Cubedo, N.; Gross, M. 4D compressive sensing holographic imaging of small moving objects with multiple illuminations. *Appl. Opt.* **2019**, *58*, G127–G134.
272. Farhadi, A.; Bedrossian, M.; Lee, J.; Ho, G.H.; Shapiro, M.G.; Nadeau, J.L. Genetically encoded phase contrast agents for digital holographic microscopy. *Nano letters* **2020**, *20*, 8127–8134.
273. Horstmeyer, R.; Heintzmann, R.; Popescu, G.; Waller, L.; Yang, C. Standardizing the resolution claims for coherent microscopy. *Nature Photonics* **2016**, *10*, 68–71.
274. He, Y.; Zhou, N.; Ziemczonok, M.; Wang, Y.; Lei, L.; Duan, L.; Zhou, R. Standardizing image assessment in optical diffraction tomography. *Opt. Lett.* **2023**, *48*, 395–398. https://doi.org/10.1364/OL.478554.
275. Kim, K.; Lee, S.; Yoon, J.; Heo, J.; Choi, C.; Park, Y. Three-dimensional label-free imaging and quantification of lipid droplets in live hepatocytes. *Scientific reports* **2016**, *6*, 36815.
276. Stasiewicz, K.; Krajewski, R.; Jaroszewicz, L.; Kujawińska, M.; Świłło, R. Influence of tapering process on changes of optical fiber refractive index distribution along a structure. *Opto-Electronics Review* **2010**, *18*, 102–109. https://doi.org/doi:10.2478/s11772-009-0030-y.
277. Fan, S.; Smith-Dryden, S.; Zhao, J.; Gausmann, S.; Schulzgen, A.; Li, G.; Saleh, B. Optical Fiber Refractive Index Profiling by Iterative Optical Diffraction Tomography. *Journal of Lightwave Technology* **2018**, *36*. https://doi.org/10.1109/JLT.2018.2876070.
278. Smith-Dryden, S.; Fan, S.; Li, G.; Saleh, B. Iterative optical diffraction tomography with embedded regularization. *Opt. Express* **2023**, *31*, 116–124. https://doi.org/10.1364/OE.466226.
279. Sullivan, A.C.; McLeod, R.R. Tomographic reconstruction of weak, replicated index structures embedded in a volume. *Opt. Express* **2007**, *15*, 14202–14212. https://doi.org/10.1364/OE.15.014202.
280. Kim, K.; Yoon, J.; Park, Y. Large-scale optical diffraction tomography for inspection of optical plastic lenses. *Opt. Lett.* **2016**, *41*, 934–937. https://doi.org/10.1364/OL.41.000934.
281. Sarmis, M.; Simon, B.; Debailleul, M.; Colicchio, B.; Georges, V.; Delaunay, J.J.; Haeberle, O. High resolution reflection tomographic diffractive microscopy. *Journal of Modern Optics* **2010**, *57*, 740–745.
282. Ziemczonok, M.; Kus, A.; Wasylczyk, P.; Kujawinska, M. 3D-printed biological cell phantom for testing 3D quantitative phase imaging systems. *Scientific Reports* **2019**, *9*, 18872. https://doi.org/10.1038/s41598-019-55330-4.
283. Krauze, W.; Kuś, A.; Ziemczonok, M.; Haimowitz, M.; Chowdhury, S.; Kujawińska, M. 3d scattering microphantom sample to assess quantitative accuracy in tomographic phase microscopy techniques. *Scientific Reports* **2022**, *12*, 19586.
284. Ziemczonok, M.; Kus, A.; Kujawinska, M. Optical diffraction tomography meets metrology—Measurement accuracy on cellular and subcellular level. *Measurement* **2022**, *195*, 111106. https://doi.org/10.1016/j.measurement.2022.111106.
285. Lee, D.; Lee, M.; Kwak, H.; Kim, Y.S.; Shim, J.; Jung, J.H.; Park, W.s.; Park, J.H.; Lee, S.; Park, Y. High-fidelity optical diffraction tomography of live organisms using iodixanol refractive index matching. *Biomedical Optics Express* **2022**, *13*, 6404–6415.
286. Bhaduri, B.; Edwards, C.; Pham, H.; Zhou, R.; Nguyen, T.H.; Goddard, L.L.; Popescu, G. Diffraction phase microscopy: principles and applications in materials and life sciences. *Adv. Opt. Photon.* **2014**, *6*, 57–119. https://doi.org/10.1364/AOP.6.000057.
287. Hugonnet, H.; Lee, M.; Shin, S.; Park, Y. Vectorial inverse scattering for dielectric tensor tomography: overcoming challenges of reconstruction of highly scattering birefringent samples. *Opt. Express* **2023**, *31*, 29654–29663. https://doi.org/10.1364/OE.494773.

288. Lee, K.; Kim, K.; Jung, J.; Heo, J.; Cho, S.; Lee, S.; Chang, G.; Jo, Y.; Park, H.; Park, Y. Quantitative phase imaging techniques for the study of cell pathophysiology: from principles to applications. *Sensors* **2013**, *13*, 4170–4191.
289. Balasubramani, V.; Kujawińska, M.; Allier, C.; Anand, V.; Cheng, C.J.; Depeursinge, C.; Hai, N.; Juodkazis, S.; Kalkman, J.; Kuś, A.; et al. Roadmap on Digital Holography-Based Quantitative Phase Imaging. *Journal of Imaging* **2021**, *7*, 252. https://doi.org/10.3390/jimaging7120252.
290. Rappaz, B.; Marquet, P.; Cuche, E.; Emery, Y.; Depeursinge, C.; Magistretti, P.J. Measurement of the integral refractive index and dynamic cell morphometry of living cells with digital holographic microscopy. *Opt. Express* **2005**, *13*, 9361–9373. https://doi.org/10.1364/OPEX.13.009361.
291. Kleiber, A.; Kraus, D.; Henkel, T.; Fritzsche, W. Tomographic imaging flow cytometry. *Lab on a Chip* **2021**, *21*, 3655–3666.
292. Pirone, D.; Mugnano, M.; Memmolo, P.; Merola, F.; Lama, G.C.; Castaldo, R.; Miccio, L.; Bianco, V.; Grilli, S.; Ferraro, P. Three-Dimensional Quantitative Intracellular Visualization of Graphene Oxide Nanoparticles by Tomographic Flow Cytometry. *Nano Letters* **2021**, *21*, 5958–5966, [https://doi.org/10.1021/acs.nanolett.1c00868]. PMID: 34232045, https://doi.org/10.1021/acs.nanolett.1c00868.
293. Isikman, S.O.; Bishara, W.; Zhu, H.; Ozcan, A. Optofluidic tomography on a chip. *Applied physics letters* **2011**, *98*, 161109.
294. Sung, Y.; Lue, N.; Hamza, B.; Martel, J.; Irimia, D.; Dasari, R.R.; Choi, W.; Yaqoob, Z.; So, P. Three-dimensional holographic refractive-index measurement of continuously flowing cells in a microfluidic channel. *Physical review applied* **2014**, *1*, 014002.
295. https://www.lynceetec.com/.
296. https://phiab.com/.
297. https://telight.eu/.
298. https://www.holmarc.com/index.php.
299. https://www.phasics.com/en/.
300. Fennema, E.; Rivron, N.; Rouwkema, J.; van Blitterswijk, C.; De Boer, J. Spheroid culture as a tool for creating 3D complex tissues. *Trends in biotechnology* **2013**, *31*, 108–115.
301. Rios, A.C.; Clevers, H. Imaging organoids: a bright future ahead. *Nature methods* **2018**, *15*, 24–26.
302. Fei, K.; Zhang, J.; Yuan, J.; Xiao, P. Present application and perspectives of organoid imaging technology. *Bioengineering* **2022**, *9*, 121.
303. Keshara, R.; Kim, Y.H.; Grapin-Botton, A. Organoid imaging: seeing development and function. *Annual review of cell and developmental biology* **2022**, *38*, 447–466.
304. Kim, U.; Quan, H.; Seok, S.H.; Sung, Y.; Joo, C. Quantitative refractive index tomography of millimeter-scale objects using single-pixel wavefront sampling. *Optica* **2022**, *9*, 1073–1083. https://doi.org/10.1364/OPTICA.464485.
305. Mudry, E.; Chaumet, P.C.; Belkebir, K.; Maire, G.; Sentenac, A. Mirror-assisted tomographic diffractive microscopy with isotropic resolution. *Opt. Lett.* **2010**, *35*, 1857–1859.
306. Zhou, N.; Sun, J.; Zhang, R.; Ye, R.; Li, J.; Bai, Z.; Zhou, S.; Chen, Q.; Zuo, C. Quasi-Isotropic High-Resolution Fourier Ptychographic Diffraction Tomography with Opposite Illuminations. *ACS Photonics* **2023**, *10*, 2461–2466.
307. Pohl, D.; Denk, W.; Lanz, M.O. Imagerecordingwithresolutionλ/20. *Appl. Phys. Lett* **1984**, *44*, 651–653.
308. Pendry, J.B. Negative refraction makes a perfect lens. *Physical review letters* **2000**, *85*, 3966.
309. Hao, X.; Kuang, C.; Liu, X.; Zhang, H.; Li, Y. Microsphere based microscope with optical super-resolution capability. *Applied Physics Letters* **2011**, *99*, 203102, [https://pubs.aip.org/aip/apl/article-pdf/doi/10.1063/1.3662010/13145406/203102_1_online.pdf]. https://doi.org/10.1063/1.3662010.
310. Micó, V.; Zheng, J.; Garcia, J.; Zalevsky, Z.; Gao, P. Resolution enhancement in quantitative phase microscopy. *Adv. Opt. Photon.* **2019**, *11*, 135–214. https://doi.org/10.1364/AOP.11.000135.
311. Astratov, V.; et al. *Label-free super-resolution microscopy*; Springer, 2019.
312. Astratov, V.N.; Sahel, Y.B.; Eldar, Y.C.; Huang, L.; Ozcan, A.; Zheludev, N.; Zhao, J.; Burns, Z.; Liu, Z.; Narimanov, E.; et al. Roadmap on Label-Free Super-Resolution Imaging. *Laser & Photonics Reviews* **2023**, p. 2200029.
313. Godavarthi, C.; Zhang, T.; Maire, G.; Chaumet, P.C.; Giovannini, H.; Talneau, A.; Belkebir, K.; Sentenac, A. Superresolution with full-polarized tomographic diffractive microscopy. *J. Opt. Soc. Am. A* **2015**, *32*, 287–292. https://doi.org/10.1364/JOSAA.32.000287.
314. Zhang, T.; Godavarthi, C.; Chaumet, P.C.; Maire, G.; Giovannini, H.; Talneau, A.; Allain, M.; Belkebir, K.; Sentenac, A. Far-field diffraction microscopy at λ/10 resolution. *Optica* **2016**, *3*, 609–612. https://doi.org/10.1364/OPTICA.3.000609.
315. Zhang, T.; Unger, K.; Maire, G.; Chaumet, P.C.; Talneau, A.; Godhavarti, C.; Giovannini, H.; Belkebir, K.; Sentenac, A. Multi-wavelength multi-angle reflection tomography. *Opt. Express* **2018**, *26*, 26093–26105. https://doi.org/10.1364/OE.26.026093.
316. Park, C.; Shin, S.; Park, Y. Generalized quantification of three-dimensional resolution in optical diffraction tomography using the projection of maximal spatial bandwidths. *J. Opt. Soc. Am. A* **2018**, *35*, 1891–1898. https://doi.org/10.1364/JOSAA.35.001891.
317. Fu, P.; Cao, W.; Chen, T.; Huang, X.; Le, T.; Zhu, S.; Wang, D.W.; Lee, H.J.; Zhang, D. Super-resolution imaging of non-fluorescent molecules by photothermal relaxation localization microscopy. *Nature Photonics* **2023**, *17*, 330–337.
318. Baffou, G.; Bon, P.; Savatier, J.; Polleux, J.; Zhu, M.; Merlin, M.; Rigneault, H.; Monneret, S. Thermal Imaging of Nanostructures by Quantitative Optical Phase Analysis. *ACS nano* **2012**, *6*, 2452–8. https://doi.org/10.1021/nn2047586.
319. Ledwig, P.; Robles, F.E. Epi-mode tomographic quantitative phase imaging in thick scattering samples. *Biomed. Opt. Express* **2019**, *10*, 3605–3621. https://doi.org/10.1364/BOE.10.003605.

320. Ledwig, P.; Robles, F.E. Quantitative 3D refractive index tomography of opaque samples in epi-mode. *Optica* **2021**, *8*, 6–14. https://doi.org/10.1364/OPTICA.410135.
321. Kang, S.; Zhou, R.; Brelen, M.; Mak, H.K.; Lin, Y.; So, P.T.; Yaqoob, Z. Mapping nanoscale topographic features in thick tissues with speckle diffraction tomography. *Light: Science & Applications* **2023**, *12*, 200.
322. Berdeu, A.; Flasseur, O.; Méès, L.; Denis, L.; Momey, F.; Olivier, T.; Grosjean, N.; Fournier, C. Reconstruction of in-line holograms: combining model-based and regularized inversion. *Opt. Express* **2019**, *27*, 14951–14968.
323. Dong, D.; Huang, X.; Li, L.; Mao, H.; Mo, Y.; Zhang, G.; Zhang, Z.; Shen, J.; Liu, W.; Wu, Z.; et al. Super-resolution fluorescence-assisted diffraction computational tomography reveals the three-dimensional landscape of the cellular organelle interactome. *Light: Science & Applications* **2020**, *9*, 11.
324. Pitrone, P.G.; Schindelin, J.; Stuyvenberg, L.; Preibisch, S.; Weber, M.; Eliceiri, K.W.; Huisken, J.; Tomancak, P. OpenSPIM: an open-access light-sheet microscopy platform. *Nature methods* **2013**, *10*, 598–599.
325. Choi, G.; Ryu, D.; Jo, Y.; Kim, Y.S.; Park, W.; seok Min, H.; Park, Y. Cycle-consistent deep learning approach to coherent noise reduction in optical diffraction tomography. *Opt. Express* **2019**, *27*, 4927–4943. https://doi.org/10.1364/OE.27.004927.
326. Lim, J.; Ayoub, A.B.; Psaltis, D. Three-dimensional tomography of red blood cells using deep learning. *Advanced Photonics* **2020**, *2*, 026001.
327. Kamilov, U.S.; Papadopoulos, I.N.; Shoreh, M.H.; Goy, A.; Vonesch, C.; Unser, M.; Psaltis, D. Learning approach to optical tomography. *Optica* **2015**, *2*, 517–522. https://doi.org/10.1364/OPTICA.2.000517.
328. Sun, Y.; Xia, Z.; Kamilov, U.S. Efficient and accurate inversion of multiple scattering with deep learning. *Opt. Express* **2018**, *26*, 14678–14688. https://doi.org/10.1364/OE.26.014678.
329. Yang, F.; an Pham, T.; Gupta, H.; Unser, M.; Ma, J. Deep-learning projector for optical diffraction tomography. *Opt. Express* **2020**, *28*, 3905–3921. https://doi.org/10.1364/OE.381413.
330. Zhou, K.C.; Horstmeyer, R. Diffraction tomography with a deep image prior. *Opt. Express* **2020**, *28*, 12872–12896. https://doi.org/10.1364/OE.379200.
331. Ryu, D.; Ryu, D.; Baek, Y.; Cho, H.; Kim, G.; Kim, Y.S.; Lee, Y.; Kim, Y.; Ye, J.C.; Min, H.S.; et al. DeepRegularizer: rapid resolution enhancement of tomographic imaging using deep learning. *IEEE Transactions on Medical Imaging* **2021**, *40*, 1508–1518.
332. Chung, H.; Huh, J.; Kim, G.; Park, Y.K.; Ye, J.C. Missing Cone Artifact Removal in ODT Using Unsupervised Deep Learning in the Projection Domain. *IEEE Transactions on Computational Imaging* **2021**, *7*, 747–758. https://doi.org/10.1109/TCI.2021.3098937.
333. Di, J.; Han, W.; Liu, S.; Wang, K.; Tang, J.; Zhao, J. Sparse-view imaging of a fiber internal structure in holographic diffraction tomography via a convolutional neural network. *Appl. Opt.* **2021**, *60*, A234–A242. https://doi.org/10.1364/AO.404276.
334. Bazow, B.; Phan, T.; Raub, C.B.; Nehmetallah, G. Three-dimensional refractive index estimation based on deep-inverse non-interferometric optical diffraction tomography (ODT-Deep). *Opt. Express* **2023**, *31*, 28382–28399. https://doi.org/10.1364/OE.491707.
335. Chung, Y.; Kim, G.; Moon, A.R.; Ryu, D.; Hugonnet, H.; Lee, M.J.; Shin, D.; Lee, S.J.; Lee, E.S.; Park, Y. Label-free histological analysis of retrieved thrombi in acute ischemic stroke using optical diffraction tomography and deep learning. *Journal of Biophotonics* **2023**, p. e202300067.